Subaru High-z Exploration of Low-Luminosity Quasars (SHELLQs). III. Star formation properties of the host galaxies at z greater than or similar to 6 studied with ALMA

Izumi, Takuma; Onoue, Masafusa; Shirakata, Hikari; Nagao, Tohru; Kohno, Kotaro; Matsuoka, Yoshiki; Imanishi, Masatoshi; Strauss, Michael A.; Kashikawa, Nobunari; Schulze, Andreas

Published in:
Publications of the Astronomical Society of Japan

DOI:
10.1093/pasj/psy026

Publication date:
2018

Publ. Astron. Soc. Japan (2018) 70 (3), 36 (1–21)
doi: 10.1093/pasj/psy026
Advance Access Publication Date: 2018 April 3

Subaru High-z Exploration of Low-Luminosity Quasars (SHELLQs). III. Star formation properties of the host galaxies at $z \gtrsim 6$ studied with ALMA

Takuma Izumi,[1,*,†] Masafusa Onoue,[1,2] Hikari Shirakata,[3] Tohru Nagao,[4] Kotaro Kohno,[5,6] Yoshiki Matsuoka,[4] Masatoshi Imanishi,[1,2] Michael A. Strauss,[1,2] Nobunari Kashikawa,[1,2] Andreas Schulze,[1,‡] John D. Silverman,[8] Seiji Fujimoto,[9] Yuichi Harikane,[9] Yoshiki Toba,[10] Hideki Umehata,[11,5] Kouichiro Nakanishi,[1,2] Jenny E. Greene,[12] Yoichi Tamura,[13] Akio Taniguchi,[5] Yuki Yamaguchi,[5] Tomotsugu Goto,[14] Yasuhiro Hashimoto,[15] Soh Ikarashi,[16] Daisuke Iono,[1,2] Kazushi Iwasawa,[17] Chien-Hsiu Lee,[1] Ryu Makiya,[8,18] Takeo Minezaki,[5] and Ji-Jia Tang[9]

[1]National Astronomical Observatory of Japan, 2-21-1 Osawa, Mitaka, Tokyo 181-8588, Japan
[2]Department of Astronomical Science, Graduate University for Advanced Studies (SOKENDAI), 2-21-1 Osawa, Mitaka, Tokyo 181-8588, Japan
[3]Department of Cosmosciences, Graduate School of Science, Hokkaido University, N10 W8, Kitaku, Sapporo, Hokkaido 060-0810, Japan
[4]Research Center for Space and Cosmic Evolution, Ehime University, 2-5 Bunkyo-cho, Matsuyama, Ehime 790-8577, Japan
[5]Institute of Astronomy, Graduate School of Science, The University of Tokyo, 2-21-1 Osawa, Mitaka, Tokyo 181-0015, Japan
[6]Research Center for the Early Universe, Graduate School of Science, The University of Tokyo, 7-3-1 Hongo, Bunkyo-ku, Tokyo 113-0033, Japan
[7]Princeton University Observatory, Peyton Hall, Princeton, NJ 08544, USA
[8]Kavli Institute for the Physics and Mathematics of the Universe (WPI), The University of Tokyo Institutes for Advanced Study, The University of Tokyo, 5-1-5 Kashiwanoha, Kashiwa, Chiba 277-8583, Japan
[9]Institute for Cosmic Ray Research, The University of Tokyo, 5-1-5 Kashiwa-no-Ha, Kashiwa, Chiba 277-8582, Japan
[10]Academia Sinica Institute of Astronomy and Astrophysics, P.O. Box 23-141, Taipei 10617, Taiwan
[11]The Open University of Japan, 2-11 Wakaba, Mihama-ku, Chiba 261-8586, Japan
[12]Department of Astrophysics, Princeton University, 4 Ivy Ln, Princeton, NJ 08544-1001, USA
[13]Division of Particle and Astrophysical Science, Graduate School of Science, Nagoya University, Furo-cho, Chikusa-ku, Nagoya, Aichi 464-8602, Japan
[14]Institute of Astronomy and Department of Physics, National Tsing Hua University, Hsinchu 30013, Taiwan
[15]Department of Earth Sciences, National Taiwan Normal University, Taipei 11677, Taiwan
[16]Kapteyn Astronomical Institute, University of Groningen, P.O. Box 800, 9700 AV Groningen, the Netherlands
[17]ICREA and Institut de Ciències del Cosmos, Universitat de Barcelona, IEEC-UB, Martí i Franquès, 1, E-08028 Barcelona, Spain

[18]Max-Planck-Institut für Astrophysik, Karl-Schwarzschild Str. 1, D-85741 Garching, Germany

*E-mail: takuma.izumi@nao.ac.jp

†NAOJ Fellow.

‡EACOA Fellow.

Received 2017 December 8; Accepted 2018 February 14

Abstract

We present our ALMA Cycle 4 measurements of the [C II] emission line and the underlying far-infrared (FIR) continuum emission from four optically low-luminosity ($M_{1450} > -25$) quasars at $z \gtrsim 6$ discovered by the Subaru Hyper Suprime Cam (HSC) survey. The [C II] line and FIR continuum luminosities lie in the ranges $L_{[\mathrm{C\,II}]} = (3.8\text{–}10.2) \times 10^8\,L_\odot$ and $L_{\mathrm{FIR}} = (1.2\text{–}2.0) \times 10^{11}\,L_\odot$, which are at least one order of magnitude smaller than those of optically-luminous quasars at $z \gtrsim 6$. We estimate the star formation rates (SFRs) of our targets as $\simeq$ 23–40 $M_\odot\,\mathrm{yr}^{-1}$. Their line and continuum-emitting regions are marginally resolved, and found to be comparable in size to those of optically-luminous quasars, indicating that their SFR or likely gas mass surface densities (key controlling parameter of mass accretion) are accordingly different. The $L_{[\mathrm{C\,II}]}/L_{\mathrm{FIR}}$ ratios of the hosts, $\simeq (2.2\text{–}8.7) \times 10^{-3}$, are fully consistent with local star-forming galaxies. Using the [C II] dynamics, we derived their dynamical masses within a radius of 1.5–2.5 kpc as $\simeq (1.4\text{–}8.2) \times 10^{10}\,M_\odot$. By interpreting these masses as stellar ones, we suggest that these faint quasar hosts are on or even below the star-forming main sequence at $z \sim 6$, i.e., they appear to be transforming into quiescent galaxies. This is in contrast to the optically-luminous quasars at those redshifts, which show starburst-like properties. Finally, we find that the ratios of black hole mass to host galaxy dynamical mass of most of the low-luminosity quasars, including the HSC ones, are consistent with the local value. The mass ratios of the HSC quasars can be reproduced by a semi-analytical model that assumes merger-induced black hole host galaxy evolution.

Key words: galaxies: high-redshift — galaxies: ISM — galaxies: quasars — galaxies: starburst — quasars: general

1 Introduction

Mass accretion on to a supermassive black hole (SMBH, with a mass of $M_{\mathrm{BH}} \gtrsim 10^6\,M_\odot$) produces an enormous amount of energy, observable as an active galactic nucleus (AGN) or a quasar (Salpeter 1964). SMBHs reside at the centers of massive galaxies, and show tight correlations between M_{BH} and the properties of the host galaxies, such as bulge stellar mass (M_{bulge}) and stellar velocity dispersion (σ_*) in the local universe (e.g., Ferrarese & Merritt 2000; Marconi & Hunt 2003; Kormendy & Ho 2013). The remarkable similarity between global star formation and mass accretion histories (Madau & Dickinson 2014, for a review), as well as correlations between luminosities associated with AGNs and with star formation in luminous systems (e.g., Lutz et al. 2010; Chen et al. 2013), support the rapid growth of SMBHs in tandem with the stellar mass build-up of galaxies.[1]

Physical mechanisms that may lead to such co-evolutionary scenarios include mergers of galaxies and subsequent AGN feedback to regulate star formation in the host. Both AGNs and star formation may be fed by a common supply of the cold interstellar medium (ISM). Hydrodynamic simulations based on this framework reproduce the observed properties of AGNs and star formation (e.g., Di Matteo et al. 2005; Hopkins et al. 2006; Li et al. 2007). Detections of massive AGN-driven outflows (e.g., Nesvadba et al. 2008; Aalto et al. 2012; Greene et al. 2012; Maiolino et al. 2012; Cicone et al. 2014; Toba et al. 2017) may also provide an important coupling between the SMBH and its host galaxy. Semi-analytic galaxy evolution models (Somerville & Davé 2015, for a review) predict intense star formation (star formation rate, SFR, reaching 100–1000 $M_\odot\,\mathrm{yr}^{-1}$) and SMBH accretion (accretion rate reaching 10 $M_\odot\,\mathrm{yr}^{-1}$) with very short characteristic time scales, on the order of 100 Myr (e.g., Hopkins et al. 2008; Volonteri et al. 2015), particularly at the peak epoch of galaxy formation ($z \sim 2$–3).

[1] Note that recent works suggest that this trend is driven by a dependence of SFR on the redshift and stellar mass (e.g., Yang et al. 2017).

One effective way to further test galaxy evolution models is to determine whether co-evolutionary scenarios have arisen in the early universe (Volonteri 2012; Gallerani et al. 2017; Valiante et al. 2017). To date, more than 200 $z \gtrsim 6$ quasars have been discovered through various wide-field optical to near-infrared surveys, including the Sloan Digital Sky Survey (SDSS; e.g., Fan et al. 2003, 2006; Jiang et al. 2016), the Canada-France High-z Quasar Survey (CFHQS; Willott et al. 2007, 2009, 2010a), the Visible and Infrared Survey Telescope for Astronomy (VISTA) Kilo-degree Infrared Galaxy (VIKING; Venemans et al. 2013, 2015b), the United Kingdom Infrared Telescope (UKIRT) Infrared Deep Sky Survey (UKIDSS; Mortlock et al. 2009, 2011), the Panoramic Survey Telescope & Rapid Response System 1 (Pan-STARRS1; e.g., Bañados et al. 2014, 2016; Mazzucchelli et al. 2017), the Dark Energy Survey (DES; e.g., Reed et al. 2017), the Dark Energy Camera Legacy Survey (DECaLS; Wang et al. 2017), those with the Suprime-Cam and the Hyper Suprime-Cam (Kashikawa et al. 2015; Matsuoka et al. 2016, 2018), and several other projects (e.g., Carnall et al. 2015; Wu et al. 2015). Most of these surveys probed the bright end of the quasar population (UV magnitude $M_{1450} \lesssim -26$) powered by almost Eddington-limited mass accretion on to massive ($\gtrsim 10^9\,M_\odot$) SMBHs (Willott et al. 2010b; De Rosa et al. 2014).

It is very challenging to detect the rest-frame optical emission from the host galaxy of a quasar at high redshift ($z \gtrsim 4$), due to surface brightness dimming and the large brightness contrast (Mechtley et al. 2012; Targett et al. 2012). However, cold gas and dust emission from star-forming regions have been used instead to probe the hosts at wavelengths that are relatively free from quasar emission. This approach has been advanced thanks to the advent of large and sensitive (sub)millimeter (hereafter submm) interferometric arrays, such as the IRAM Plateau de Bure interferometer (now NOEMA) and the Atacama Large Millimeter/submillimeter Array (ALMA). Observations of galaxies hosting luminous $M_{1450} < -26$ quasars at $z \gtrsim 6$ have revealed large reservoirs of dust ($\sim 10^8\,M_\odot$) and cold molecular gas ($\sim 10^{10}\,M_\odot$) with high far-infrared (FIR) luminosities ($L_{\rm FIR} > 10^{12}\,L_\odot$), indicating vigorous star formation activity (SFR $\gtrsim$ 100–1000 $M_\odot\,{\rm yr}^{-1}$) coeval with the central AGNs (e.g., Bertoldi et al. 2003a, 2003b; Petric et al. 2003; Priddey et al. 2003, 2008; Robson et al. 2004; Walter et al. 2004; Wang et al. 2007, 2008, 2010, 2011a, 2011b; Omont et al. 2013; Gallerani et al. 2014; Stefan et al. 2015), and placing tight constraints on early star formation and dust formation histories (e.g., Calura et al. 2014; Valiante et al. 2014).

Interferometric studies of the strong 157.74 μm [C II] $^2{\rm P}_{3/2} \rightarrow {}^2{\rm P}_{1/2}$ emission line (rest frequency 1900.539 GHz), which is the principal coolant of photodissociation regions of galaxies (Stacey et al. 1991; Hollenbach & Tielens 1999), has also been an important tracer of the hosts of high-z quasars. Such observations have revealed vigorous star-forming activity located in relatively compact regions (a few kpc in diameter) as well as the cold gas dynamics of $z \gtrsim 6$ galaxies, hosting not only luminous quasars (Maiolino et al. 2005; Wang et al. 2013, 2016; Bañados et al. 2015; Venemans et al. 2016, 2017; Decarli et al. 2017, 2018; Mazzucchelli et al. 2017) but also less luminous ($M_{1450} \gtrsim -25$) quasars (Willott et al. 2013, 2015, 2017). These dynamical studies revealed that $z \gtrsim 6$ luminous quasars have, on average, 10 times more massive SMBHs than the local co-evolutionary relations for a given velocity dispersion σ or dynamical mass of the host, implying that SMBHs were formed significantly earlier than their hosts (e.g., Lamastra et al. 2010).[2]

However, there would be a selection bias for high-redshift quasars towards more luminous objects or more massive SMBHs if the underlying $M_{\rm BH}$ distribution has a large scatter for a given galaxy mass (Willott et al. 2005; Lauer et al. 2007; Schulze & Wisotzki 2014). Therefore, it is vital to probe lower-luminosity quasars and their hosts to obtain an unbiased view of early co-evolution that accounts for the bulk of the SMBH population at that time (e.g., Schramm & Silverman 2013). Indeed, studies of less-luminous ($M_{1450} \gtrsim -25$) CFHQS quasars with lower-mass SMBHs ($\sim 10^8\,M_\odot$) have revealed that their dynamical masses are well matched to those of local galaxies (Willott et al. 2015, 2017). This lower-luminosity regime is now being extensively explored as part of our wide-field and sensitive survey with the Hyper Suprime-Cam (HSC: Miyazaki et al. 2012, 2018; Kawanomoto et al. 2017; Komiyama et al. 2018; Furusawa et al. 2018) mounted on the Subaru telescope: we have discovered more than 50 quasars at $z \gtrsim 6$ (Matsuoka et al. 2016, 2018). We have organized an extensive multiwavelength follow-up consortium: Subaru High-z Exploration of Low-Luminosity Quasars (SHELLQs).

In this paper, we report ALMA Cycle 4 observations of the [C II] 158-μm emission line and the underlying rest-frame FIR continuum emission of four HSC quasar host galaxies at $z \gtrsim 6$ (table 1), i.e., J0859+0022 (Lyα-based redshift $z_{{\rm Ly}\alpha} = 6.39$), J1152+0055 ($z_{{\rm Ly}\alpha} = 6.37$), J2216−0016 ($z_{{\rm Ly}\alpha} = 6.10$), and J1202−0057 ($z_{{\rm Ly}\alpha} = 5.93$), originally discovered by Matsuoka et al. (2016). These HSC quasars are ∼3–4 magnitudes fainter than most of the $z \gtrsim 6$ luminous-end quasars ($M_{1450} < -26$) so far studied in the rest-FIR, and are comparably faint to the low-luminosity CFHQS quasars at $z \gtrsim 6$ (Willott et al. 2007, 2010a). We

[2] [C II] velocity dispersion ($\sigma_{\rm [C\,II]}$) is widely used as a surrogate for a stellar velocity dispersion in the case of high-z quasars.

Table 1. Description of our sample and the ALMA observations.*

	J0859+0022	J1152+0055	J2216−0016	J1202−0057
RA (J2000.0)	$08^{h}59^{m}07\overset{s}{.}19$	$11^{h}52^{m}21\overset{s}{.}27$	$22^{h}16^{m}44\overset{s}{.}47$	$12^{h}02^{m}46\overset{s}{.}37$
Dec (J2000.0)	$+00°22'55\overset{''}{.}9$	$+00°55'36\overset{''}{.}6$	$-00°16'50\overset{''}{.}1$	$-00°57'01\overset{''}{.}7$
$z_{\mathrm{Ly}\alpha}$	6.39	6.37	6.10	5.93
M_{1450}	−24.09	−25.31	−23.82	−22.83
Number of antennas	45	45	40–41	42–45
Baseline (m)	15.1–704.1	15.1–704.1	15.1–704.1	15.1–492.0
On-source time (min)	105	17	99	205
Bandpass calibrator	J0854+2006	J1229+0203	J2148+0657	J1229+0203
Complex gain calibrator	J0909+0121	J1220+0203	J2226+0052	J1220+0203
Flux calibrator	J0750+1231, J0854+2006	J1229+0203	J2148+0657	J1229+0203
T_{sys} (K)	∼ 80–100	∼ 70	∼ 80–110	∼ 90–150
[C II] cube				
Beam size:	$0\overset{''}{.}64 \times 0\overset{''}{.}47$	$0\overset{''}{.}52 \times 0\overset{''}{.}47$	$0\overset{''}{.}54 \times 0\overset{''}{.}43$	$0\overset{''}{.}79 \times 0\overset{''}{.}71$
Position angle (east of north)	$60\overset{\circ}{.}9$	$72\overset{\circ}{.}3$	$-62\overset{\circ}{.}2$	$79\overset{\circ}{.}4$
rms noise per 50 km s^{-1} (mJy beam^{-1})	0.12	0.24	0.18	0.12
rms noise per 50 km s^{-1} (mJy beam^{-1}; $1\overset{''}{.}5$ aperture)	0.25	0.52	0.41	0.21
Continuum map				
Observed continuum frequency (GHz)	249.5	250.0	259.6	265.5
Beam size:	$0\overset{''}{.}56 \times 0\overset{''}{.}50$	$0\overset{''}{.}54 \times 0\overset{''}{.}50$	$0\overset{''}{.}56 \times 0\overset{''}{.}45$	$0\overset{''}{.}81 \times 0\overset{''}{.}73$
Position angle (east of north)	$61\overset{\circ}{.}2$	$70\overset{\circ}{.}1$	$-62\overset{\circ}{.}2$	$80\overset{\circ}{.}0$
rms noise: (μJy beam^{-1})	9.5	20.7	13.2	8.8
rms noise: (μJy beam^{-1}; $1\overset{''}{.}5$ aperture)	23.4	32.3	27.1	12.2

*Rest-frame UV properties are adapted from Matsuoka et al. (2016, 2018).

describe our observations in section 2. The observed properties of both [C II] line and FIR continuum emission are presented in section 3. Then we discuss the star-forming nature of the HSC quasar hosts and the less-biased early co-evolution in section 4, and present our conclusions in section 5. Throughout the paper, we assume the standard cosmology with $H_0 = 70\,\mathrm{km\,s^{-1}\,Mpc^{-1}}$, $\Omega_{\mathrm{M}} = 0.3$, and $\Omega_{\Lambda} = 0.7$.

2 Observations and data reduction

Four $z \gtrsim 6$ HSC quasars were observed during ALMA Cycle 4 (ID = 2016.1.01423.S, PI: T. Izumi) at band 6 between 2016 December 2 and 2017 April 13. Our observations are summarized in table 1, along with the basic target information. These observations were conducted in a single pointing (two side-band dual-polarization mode) with ∼25″ diameter field of view, which corresponds to ∼140 kpc at the source redshifts (1″ corresponds to 5.5–5.8 kpc). The phase tracking centers were set to the optical quasar locations (Matsuoka et al. 2016). The absolute positional uncertainty is ∼0″.1 according to the ALMA Knowledgebase.[3] With the minimum baseline length (15.1 m), the maximum recoverable scale of our observations is ∼9″.5.

The receivers were tuned to cover the redshifted [C II] line emissions, the frequencies of which were estimated from the measured redshifts of Lyα. The total bandwidth of these observations was ∼7.5 GHz, divided into four spectral windows of width 1.875 GHz. The original spectral resolution was 3.906 MHz (4.4–4.8 km s^{-1}), but 11–12 channels were binned to improve the signal-to-noise ratio (S/N), resulting in a final common velocity resolution of $\simeq 50\,\mathrm{km\,s^{-1}}$.

Reduction and calibration of the data were performed with the Common Astronomy Software Applications (CASA) package (McMullin et al. 2007) version 4.7 in the standard manner. All images were reconstructed with the CASA task `clean` (gain = 0.1, weighting = briggs, robust = 0.5). The achieved synthesized beams and rms sensitivities at a velocity resolution of 50 km s^{-1} are summarized in

[3] ⟨https://help.almascience.org/index.php?/Knowledgebase/List⟩.

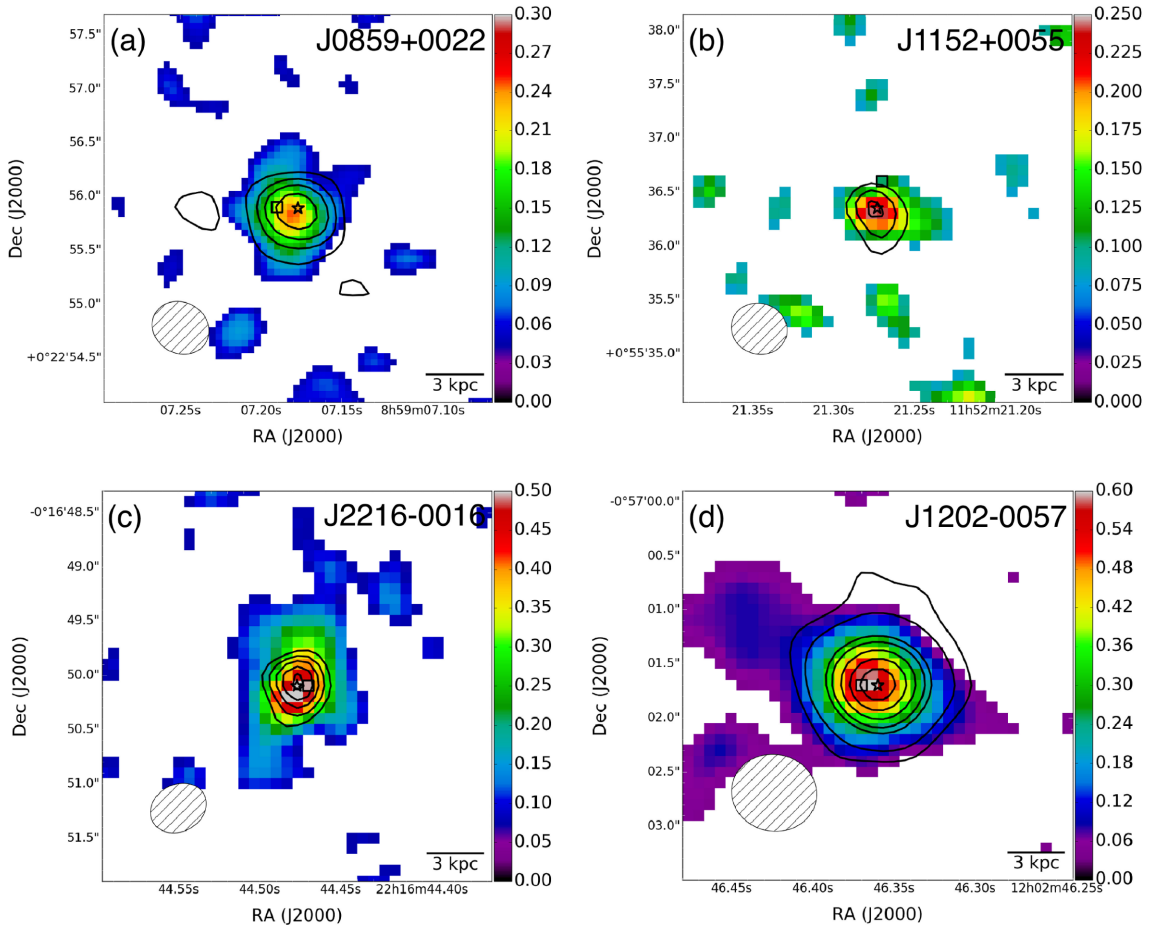

Fig. 1. Spatial distributions of the velocity-integrated [C II] line (i.e., 0th moment map; color scale in units of Jy beam^{-1} km s^{-1}) and rest-frame FIR continuum (contours) emission of the HSC quasars, (a) J0859+0022, (b) J1152+0055, (c) J2216−0016, and (d) J1202−0057, visualized with the original resolutions. The synthesized beams are in the bottom left-hand corners. The central stars and the squares mark the continuum peaks at the rest-frame FIR (this work) and the rest-frame UV (Matsuoka et al. 2016), respectively, which coincide within the positional uncertainties in every case. Contours indicate: (a) 3σ, 5σ, 7σ, 10σ ($1\sigma = 9.5\,\mu$Jy beam^{-1}), (b) 3σ, 4σ, 5σ ($1\sigma = 20.7\,\mu$Jy beam^{-1}), (c) 3σ, 4σ, 5σ, 6σ, 7σ ($1\sigma = 13.2\,\mu$Jy beam^{-1}), and (d) 3σ, 5σ, 10σ, 12σ, 15σ, 18σ, 21σ ($1\sigma = 8.8\,\mu$Jy beam^{-1}). The rms sensitivity of the velocity-integrated [C II] emission is (a) 0.036, (b) 0.053, (c) 0.047, and (d) 0.027 Jy beam^{-1} km s^{-1}, respectively. Pixels below these 1σ levels were masked in the color maps. (Color online)

table 1. All channels free of line emissions (∼7.5 GHz) were averaged to generate a continuum map for each source. The synthesized beams and rms sensitivities of these maps are also listed in table 1. For each source, the continuum emission was subtracted in the (u, v) plane before making the line cube. We used line intensities corrected for the primary beam attenuation for quantitative discussions, but this had a negligible effect, as all emission was found to lie in the central $r \lesssim 1\farcs5$ of each image. The pixel scale of all maps in this paper is set to $0\farcs1$. Only statistical errors are displayed, unless otherwise mentioned. Note that the systematic uncertainty of the absolute flux calibration at ALMA band 6 is 10%, according to the ALMA Cycle 4 Proposer's Guide.[4]

[4] ⟨https://almascience.nao.ac.jp/proposing/documents-and-tools/cycle4/alma-proposers-guide⟩.

3 Results

Figure 1 shows the spatial distribution of the velocity-integrated (i.e., 0th moment) [C II] line and $\lambda_{\rm obs} \simeq 1.2$ mm (or $\lambda_{\rm rest} \simeq 158\,\mu$m) continuum emission of the HSC quasars. Both line and continuum emission were clearly detected for all sources, with no apparent spatial offset among the line, 1.2 mm continuum, and optical centroids. Note that the velocity ranges which encompass the [C II] line emission were integrated over (using CASA task `immoments`) to make the moment-0 maps. The emission appears to be slightly extended relative to the synthesized beams. Given this, we decided to measure the rest-frame FIR properties with a common $1\farcs5$ diameter circular aperture. The rms sensitivities within this aperture are also listed in table 1. The resultant properties are summarized in table 2.

Table 2. Rest-frame FIR properties of the HSC quasars.*

	J0859+0022	J1152+0055	J2216−0016	J1202−0057
$z_{[\mathrm{C\,II}]}$	6.3903 ± 0.0005	6.3637 ± 0.0005	6.0962 ± 0.0003	5.9289 ± 0.0002
$\mathrm{FWHM}_{[\mathrm{C\,II}]}$ (km s^{-1})	346 ± 46	192 ± 45	356 ± 33	335 ± 24
$S_{[\mathrm{C\,II}]}$ (Jy km s^{-1})	0.45 ± 0.05	0.37 ± 0.08	1.05 ± 0.08	0.68 ± 0.04
$L_{[\mathrm{C\,II}]}$ ($10^8\,L_\odot$)	4.6 ± 0.5	3.8 ± 0.8	10.2 ± 0.8	6.2 ± 0.4
$f_{1.2\mathrm{mm}}$ (μJy)	157 ± 23	189 ± 32	136 ± 27	246 ± 12
$\mathrm{EW}_{[\mathrm{C\,II}]}$ (μm)	1.50 ± 0.28	1.02 ± 0.27	4.08 ± 0.87	1.44 ± 0.11
$\mathrm{SFR}_{[\mathrm{C\,II}]}$ ($M_\odot$ yr^{-1})	31 ± 4	25 ± 5	67 ± 5	42 ± 3
		$T_\mathrm{d} = 47$ K, $\beta = 1.6$		
L_FIR ($10^{11}\,L_\odot$)	3.4 ± 0.5	4.1 ± 0.7	2.8 ± 0.6	4.8 ± 0.2
L_TIR ($10^{11}\,L_\odot$)	4.8 ± 0.7	5.8 ± 1.0	3.9 ± 0.8	6.7 ± 0.3
$\mathrm{SFR}_\mathrm{TIR}$ ($M_\odot$ yr^{-1})	71 ± 10	86 ± 14	58 ± 11	100 ± 5
M_dust ($10^7\,M_\odot$)	2.4 ± 0.4	2.9 ± 0.5	2.0 ± 0.4	3.4 ± 0.2
$L_{[\mathrm{C\,II}]}/L_\mathrm{FIR}$ (10^{-3})	1.4 ± 0.3	0.9 ± 0.2	3.7 ± 0.8	1.3 ± 0.1
		$T_\mathrm{d} = 35$ K, $\beta = 1.6$		
L_FIR ($10^{11}\,L_\odot$)	1.5 ± 0.2	1.7 ± 0.3	1.2 ± 0.2	2.0 ± 0.1
L_TIR ($10^{11}\,L_\odot$)	1.9 ± 0.3	2.3 ± 0.4	1.5 ± 0.3	2.7 ± 0.1
$\mathrm{SFR}_\mathrm{TIR}$ ($M_\odot$ yr^{-1})	28 ± 4	34 ± 6	23 ± 5	40 ± 2
M_dust ($10^7\,M_\odot$)	5.0 ± 0.7	6.0 ± 1.0	4.1 ± 0.8	7.1 ± 0.3
$L_{[\mathrm{C\,II}]}/L_\mathrm{FIR}$ (10^{-3})	3.2 ± 0.6	2.2 ± 0.6	8.7 ± 1.8	3.1 ± 0.2

*These were measured with a common 1.″5 aperture. The (far-)infrared luminosities were estimated with a graybody spectrum model. $\mathrm{SFR}_{[\mathrm{C\,II}]}/M_\odot\,\mathrm{yr}^{-1} = 1.0 \times 10^{-7}\,(L_{[\mathrm{C\,II}]}/L_\odot)^{0.98}$ (De Looze et al. 2011). $\mathrm{SFR}_\mathrm{TIR}/M_\odot\,\mathrm{yr}^{-1} = 1.49 \times 10^{-10} L_\mathrm{TIR}/L_\odot$ (Murphy et al. 2011).

3.1 [C II] line properties

Figure 2 shows the [C II] line spectra measured with the 1.″5 diameter aperture. We fitted each continuum-subtracted spectrum with a single-Gaussian profile to extract the redshift ($z_{[\mathrm{C\,II}]}$), line width (full width at half maximum = $\mathrm{FWHM}_{[\mathrm{C\,II}]}$), and the velocity-integrated line flux ($S_{[\mathrm{C\,II}]}$) of each source, as listed in table 2. The line profiles were fitted well with the single Gaussians (i.e., we found no strong indication of [C II] outflows), although we will examine the case of a double-Gaussian fit to J2216−0016 in subsection 3.5, as it is a broad absorption line quasar clearly showing nuclear outflows associated with it. However, as further observations are needed to confirm the necessity of the double-Gaussian fit, we use the results from the single-Gaussian fit to be consistent across the sample.

The velocity centroids of the [C II] lines show no significant offset from those determined based on their Lyα emission lines (Matsuoka et al. 2016), even though the latter could have considerable uncertainties, due to intergalactic absorption (e.g., Eilers et al. 2017). On the other hand, some quasars show $\gtrsim 500$ km s^{-1} shifts (mostly blueshifts) of the Mg II line relative to the [C II] line (e.g., Bañados et al. 2015; Willott et al. 2015; Venemans et al. 2016; Wang et al. 2016; Trakhtenbrot et al. 2017), suggesting fast ionized outflows at the nuclei of those quasars. The difference between $z_{[\mathrm{C\,II}]}$ and $z_{\mathrm{Ly}\alpha}$ is a measure of the neutral fraction of the intergalactic medium at $z > 6$, but this analysis is beyond the scope of this paper. The FWHMs of our HSC quasars are comparable to those of previously observed high-redshift quasars (e.g., Wang et al. 2013; Willott et al. 2015; Venemans et al. 2016), which lie in the range of ∼200–500 km s^{-1}.

We also calculated the [C II] line luminosities of our sources with the standard equation of $L_{[\mathrm{C\,II}]} = 1.04 \times 10^{-3} S_{[\mathrm{C\,II}]} \nu_\mathrm{rest} (1 + z_{[\mathrm{C\,II}]})^{-1} D_L^2$ (Solomon & Vanden Bout 2005). Here, $L_{[\mathrm{C\,II}]}$ is the [C II] line luminosity in units of $L_\odot$, ν_rest is in units of GHz, $S_{[\mathrm{C\,II}]}$ is in units of Jy km s^{-1}, and D_L is the luminosity distance in units of Mpc. We obtained $L_{[\mathrm{C\,II}]} \simeq (4\text{–}10) \times 10^8\,L_\odot$, with only the most luminous J2216−0016 reaching $10^9\,L_\odot$. This is in clear contrast to the corresponding values for optically-luminous $z \gtrsim 6$ quasars, $L_{[\mathrm{C\,II}]} \simeq (1\text{–}10) \times 10^9\,L_\odot$ (Maiolino et al. 2005; Venemans et al. 2012, 2016, 2017; Wang et al. 2013, 2016; Bañados et al. 2015). At these redshifts, FIR/submm-selected dusty starburst galaxies also exhibit $L_{[\mathrm{C\,II}]} \gtrsim (1\text{–}10) \times 10^9\,L_\odot$ (Riechers et al. 2013; Strandet et al. 2017). On the other hand, the $L_{[\mathrm{C\,II}]}$ values for the HSC quasars are comparable to those of the less-luminous CFHQS quasars (Willott et al. 2013, 2015, 2017), as well as to those of UV/optically-selected galaxies at $z > 6$ (e.g., Aravena et al. 2016).

If we attribute the heating source of the [C II] emission to young stars, as is commonly assumed, the above trend

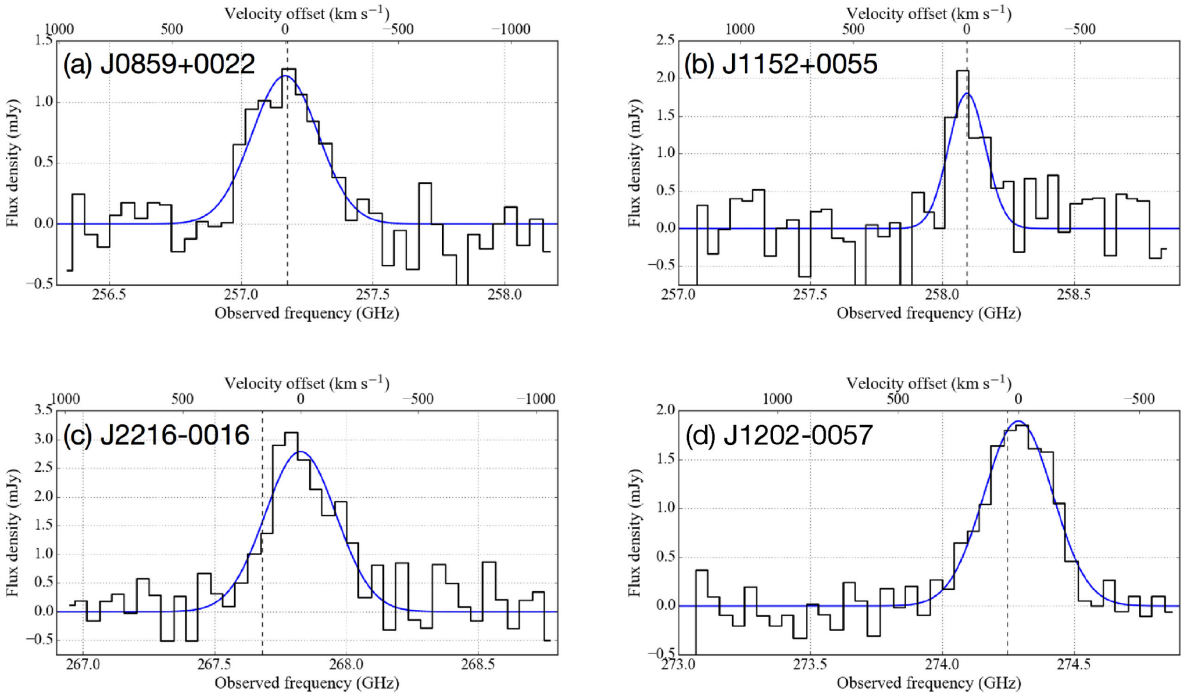

Fig. 2. [C II] line spectrum of the four HSC quasars obtained with ALMA. The curves indicate the best-fitting single-Gaussian profiles. The upper axis in each panel is the velocity offset from the [C II] Gaussian peak. The expected [C II] frequencies from the Lyα-based redshifts are indicated by the vertical dashed lines. (Color online)

indicates a lower SFR in the host galaxies of less-luminous quasars. We then applied the relation in De Looze et al. (2011) of $\mathrm{SFR}_{[\mathrm{C\,II}]}/M_\odot\ \mathrm{yr}^{-1} = 1.0 \times 10^{-7}(L_{[\mathrm{C\,II}]}/L_\odot)^{0.98}$ to derive the values listed in table 2. This relation, with a dispersion of $\sim$0.3 dex (this is not included in the errors of the derived SFR), is calibrated with the Kroupa initial mass function (IMF: Kroupa 2001) for galaxies of $L_{\mathrm{FIR}} \lesssim 10^{12}\,L_\odot$. It is consistent with that in Sargsyan et al. (2014), which is independently calibrated with infrared [Ne II] and [Ne III] lines (see also Herrera-Camus et al. 2015). The possible contribution of quasars to the [C II] line heating (e.g., Stacey et al. 2010) is neglected here, as (i) the so-called [C II]-deficit that would imply an influence of AGNs on the FIR properties in cases of quasars was not seen in our sample (subsection 4.1), and (ii) the measured [C II] equivalent widths of the HSC quasars ($\mathrm{EW}_{[\mathrm{C\,II}]}$; table 2) are consistent with the typical values of local starburst galaxies (e.g., Díaz-Santos et al. 2013; Sargsyan et al. 2014). J2216−0016 even has an EW at the high-end of the range for local galaxies ($4.08 \pm 0.87\,\mu$m). Furthermore, a possible dependence of [C II] strength on the gas-phase metallicity (Harikane et al. 2017) is also neglected as the HSC quasar hosts are found to be massive (section 4), implying that they are evolved systems. The derived SFRs (25–$67\,M_\odot\,\mathrm{yr}^{-1}$), and the $L_{[\mathrm{C\,II}]}$ values themselves, are well within the range of local luminous infrared galaxy (LIRG)-class systems, (e.g., De Looze et al. 2011; Díaz-Santos et al. 2013; Sargsyan et al. 2014), although the HSC quasars are located at $z \gtrsim 6$.

3.2 FIR continuum properties

The observed $\lambda = 1.2$ mm continuum emission ($f_{1.2\,\mathrm{mm}}$; table 2) is primarily emitted from the thermal dust (e.g., Yun et al. 2000; Carilli et al. 2001; Beelen et al. 2006). We used this to derive the FIR (42.5–122.5 μm; Helou et al. 1988) continuum luminosity L_{FIR}, which traces SFR if we assume that the cold dust is primarily heated by young stars (e.g., Kennicutt 1998). This assumption is thought to be valid for quasars (e.g., Schweitzer et al. 2006; Leipski et al. 2014), although contrary arguments have also been proposed (e.g., Symeonidis et al. 2016; Symeonidis 2017). In practice, the intrinsic (i.e., AGN-heated) FIR spectral shape of quasars would vary from source to source (Lyu & Rieke 2017), but handling of this effect is quite challenging at the moment.

To compute L_{FIR}, we first adopted an optically thin gray-body spectrum model with dust temperature $T_{\mathrm{d}} = 47$ K and emissivity index $\beta = 1.6$ (emissivity $\propto \nu^\beta$) to be consistent with previous $z > 6$ quasar studies (e.g., Wang et al. 2013; Willott et al. 2015; Venemans et al. 2016). These fixed parameters are based on the mean spectral energy distribution of high-redshift optically/FIR-luminous quasars at $1.8 < z < 6.4$ (Beelen et al. 2006, see also Leipski et al.

2014). However, it is uncertain whether these values are applicable to the much less luminous (at both the optical and FIR bands) HSC quasars, which should be studied further with future multiwavelengths observations. We also explore the consequence of lower $T_{\rm d}$ below, which may be more realistic.

We also considered the influence of the cosmic microwave background (CMB) on the submm observations at high redshifts (da Cunha et al. 2013), as the CMB provides an additional source of dust heating. However, those effects are negligible as long as we adopt $T_{\rm d} \gtrsim 35$ K. We thus do not make any correction to the observed submm fluxes in this study: we should revise our estimation on, e.g., $L_{\rm FIR}$, once an accurate $T_{\rm d}$ is obtained.

The resultant $L_{\rm FIR}$ ($T_{\rm d} = 47$ K) values are listed in table 2. They all fall within a relatively narrow range, $\simeq$ (3–5) $\times$ $10^{11}\,L_{\odot}$, corresponding to the luminosity range of LIRGs. This is consistent with the [C II]-based results, where we also found LIRG-like line luminosities. The $L_{\rm FIR}$ of our HSC quasars are then much fainter than the $z \gtrsim 6$ optically-luminous quasars by factors of $\simeq$ 10–100 (e.g., Wang et al. 2007, 2008, 2011a). On the other hand, their $L_{\rm FIR}$ are higher than some optically-selected normal galaxies (not AGNs) at $z \sim 6$ that are not detected at FIR even with the high sensitivity of ALMA (Capak et al. 2015), indicating that quasars are indeed dust-enriched systems.

The SFR were estimated simply by (i) extending the graybody spectrum to the total IR (TIR: 8–1000 μm, table 2) range, (ii) assuming that star-forming activity fully accounts for the TIR, and (iii) applying the conversion, $\mathrm{SFR}/M_{\odot}\,\mathrm{yr}^{-1} = 1.49 \times 10^{-10}\,L_{\rm TIR}/L_{\odot}$ (Murphy et al. 2011). This conversion is also grounded on the Kroupa IMF and is in accord with other studies (e.g., Kennicutt 1998) after accounting for the differing IMFs assumed therein. We found SFR =58–100 $M_{\odot}\,\mathrm{yr}^{-1}$ for our sources. Note that we here neglected a contribution of UV luminosity to the SFR estimation as the UV-to-IR luminosity ratio is small for massive star-forming galaxies, such as those with stellar masses of $\gtrsim 10^{10}\,M_{\odot}$ (e.g., Whitaker et al. 2012; Dunlop et al. 2017), which would be the case for $z \gtrsim 6$ quasars (see also section 4). We also derived the cold dust mass ($M_{\rm dust}$), using $M_{\rm dust} = L_{\rm FIR}/(4\pi \int \kappa_{\nu} B_{\nu} d\nu)$ with a mass absorption coefficient $\kappa_{\nu} = \kappa_0\ (\nu/250\,\mathrm{GHz})^{\beta}$ and $\kappa_0 = 0.4\,\mathrm{cm}^2\,\mathrm{g}^{-1}$ (Alton et al. 2004; Beelen et al. 2006). Assuming $T_{\rm d} = 47$ K, we found $M_{\rm dust} \simeq$ (2–3) $\times$ $10^7\,M_{\odot}$. As expected from our methodology, the values of SFR and $M_{\rm dust}$ are comparable to those observed in local LIRG-class systems (e.g., U et al. 2012; Tateuchi et al. 2015).

However, the above TIR-based SFRs ($\mathrm{SFR}_{\rm TIR}$) are systematically larger than the [C II]-based SFRs($\mathrm{SFR}_{\rm [C\,II]}$) except for the case of J2216−0016. This could not be due to significant AGN contamination to the dust heating, as

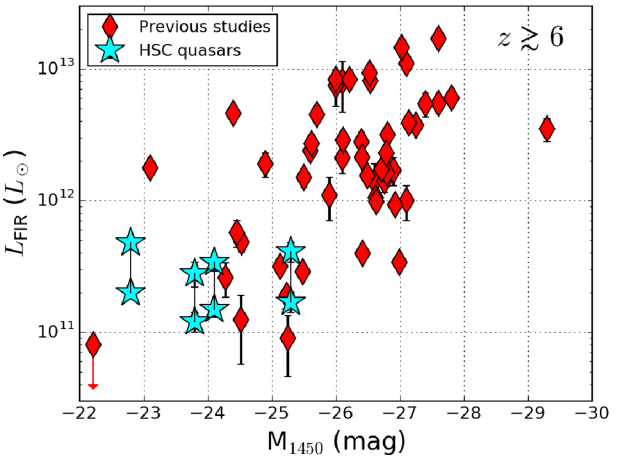

Fig. 3. FIR luminosity ($L_{\rm FIR}$) as a function of quasar UV absolute magnitude (M_{1450}) for our HSC quasars (cyan stars) along with previously studied $z \gtrsim 6$ quasars (Maiolino et al. 2005; Venemans et al. 2012, 2016, 2017; Wang et al. 2013, 2016; Willott et al. 2013, 2015, 2017; Bañados et al. 2015, 2018; Decarli et al. 2017, 2018; Mazzucchelli et al. 2017). $L_{\rm FIR}$ is calculated with the graybody model with $T_{\rm d} = 47$ K and $\beta = 1.6$. For the HSC quasars, we also plot the cases with $T_{\rm d} = 35$ K. This figure enhances the fact that we are probing a lower-luminosity population in terms of both optical and FIR luminosity at $z \gtrsim 6$ with the HSC survey. (Color online)

the observed $\mathrm{EW}_{\rm [C\,II]}$ values are comparable to those for star-forming LIRGs. On the other hand, $T_{\rm d}$ itself is usually very uncertain even among star-forming galaxies: our less-luminous HSC quasars (at both the optical and FIR bands) may have lower $T_{\rm d}$ than the luminous-end quasars. If we adopt $T_{\rm d} = 35$ K instead, which is a typical value observed in local LIRGs (e.g., U et al. 2012) and SMGs at $z \sim$ 1–3 that have LIRG-class or Ultra-infrared luminous Galaxy (ULIRG)-class $L_{\rm FIR}$ (e.g., Chapman et al. 2005; Kovács et al. 2006; Coppin et al. 2008), the resultant $L_{\rm FIR}$ is reduced by $\simeq$ 50%–60%, by fixing β to 1.6. In this case (table 2), the relevant FIR continuum properties are then $L_{\rm FIR} \simeq$ (1–2) $\times$ $10^{11} L_{\odot}$, $\mathrm{SFR}_{\rm TIR} =$ 23–40 $M_{\odot}\,\mathrm{yr}^{-1}$, $M_{\rm dust} \simeq$ (4–7) $\times$ $10^7\,M_{\odot}$, respectively. The $\mathrm{SFR}_{\rm TIR}$ now agrees better with $\mathrm{SFR}_{\rm [C\,II]}$ for J0859+0022, J1152+0055, and J1202−0057, although the discrepancy in $L_{\rm FIR}$ between the HSC quasars and the optically-luminous quasars becomes larger (figure 3).

3.3 Spatial extent of the star-forming region

The spatial extent of the star-forming region of each source was estimated by applying a two-dimensional Gaussian fit to both the [C II] integrated intensity and the continuum maps, using the CASA task `IMFIT`.[5] This method (i.e., image-plane fitting) is consistent with those used in the previous submm studies on quasar host galaxies, which enables

[5] This region could have a different distribution from the already existing stellar component (see recent discussion in, e.g., Simpson et al. 2015).

Table 3. Spatial extent of the star-forming region of the HSC quasars.

Name	Size ([C II] FWHM)	Size (continuum FWHM)
J0859+0022	(0.″51 ± 0.″15) × (0.″33 ± 0.″19) (2.8 ± 0.8) kpc × (1.8 ± 1.0) kpc	(0.″39 ± 0.″16) × (0.″27 ± 0.″15) (2.2 ± 0.9) kpc × (1.5 ± 0.8) kpc
J1152+0055	(0.″58 ± 0.″20) × (0.″25 ± 0.″13) (3.0 ± 1.1) kpc × (1.4 ± 0.7) kpc	(0.″61 ± 0.″19) × (0.″24 ± 0.″17) (3.4 ± 1.0) kpc × (1.3 ± 0.9) kpc
J2216−0016	(0.″91 ± 0.″15) × (0.″44 ± 0.″12) (5.2 ± 0.8) kpc × (2.5 ± 0.7) kpc	(0.″52 ± 0.″16) × (0.″41 ± 0.″23) (2.9 ± 0.9) kpc × (2.3 ± 1.3) kpc
J1202−0057	(0.″45 ± 0.″12) × (0.″27 ± 0.″19) (2.6 ± 0.7) kpc × (1.5 ± 1.1) kpc	(0.″47 ± 0.″10) × (0.″42 ± 0.″14) (2.7 ± 0.6) kpc × (2.4 ± 0.8) kpc

us a fair comparison of our results with them. We note another possibility to estimate the source sizes by using *uv*-plane fitting, but such a method only applies for data with decent S/N (∼10–15, e.g., Ikarashi et al. 2015), which is not the case for our work.

The original resolution data (table 1 and figure 1) were used for our size measurements with 3σ clipping to avoid noise contamination. The resultant values are listed in table 3: the [C II] emitting regions have sizes of FWHM ∼2.6–5.2 kpc, while the associated uncertainties are still large.

We found good consistency between the [C II]-based sizes and continuum-based sizes within the uncertainties, except for the case of J2216−0016, where the [C II]-based size is ∼1.8 times larger than the continuum-based size along its major axis (see also figure 1 and subsection 3.5). Interestingly, the spatial extents of our HSC quasars (even including J2216−0016) are comparable to those of the $z \gtrsim 6$ optically-luminous quasars observed at submm, having $M_{\rm dust} \sim$ several $\times\ 10^8\,M_\odot$ (e.g., Wang et al. 2013; Venemans et al. 2016), within the uncertainties. Thus, an order of magnitude difference in SFR (or $M_{\rm dust}$) between these populations could directly translate to a similar level of difference in the SFR (or ISM mass under a certain gas-to-dust mass ratio, e.g., Draine et al. 2007) *surface density*. Indeed, gas mass surface density around an AGN is a key parameter for the black hole mass accretion, as it controls the gravitational instability therein, which can transport gas inward (e.g., Hopkins & Quataert 2010).

3.4 Other emitters within the fields

We searched for other emitters within the fields of view (FoV; HPBW $\simeq 25''$) of each source. The line cubes and the continuum maps with the original angular resolutions were used here.

3.4.1 [C II] emitters adjacent to the quasars?

We first searched for [C II] emitters within the FoVs, particularly those associated with the central quasars. We applied the procedure described in Yamaguchi et al. (2017) to our continuum-subtracted cubes. To this end, spectral windows (1.875 GHz width with $\simeq$ 43 MHz binning) that contain the quasar [C II] emission were surveyed. We used the `CLUMPFIND` software (Williams et al. 1994) to search for line emitters other than the HSC quasars themselves with a peak $S/N \geq 5$. The relevant parameters were $\Delta S = 1\sigma$ and $S_{\rm start} = 3\sigma$, where ΔS is the contouring interval, and $S_{\rm start}$ is the starting contour level. To avoid spurious detections, we rejected candidates that do not show $S/N \geq 3$ emission in any of the channels adjacent to the peak ones. The frequency resolution (43 MHz) or the velocity resolution of 50 km s^{-1} for objects near the quasar redshifts would be sufficient to resolve a typical line width (∼150–200 km s^{-1}; e.g., Aravena et al. 2016) of galaxies at $z \sim 6$ into several spectral elements.

As a result, we did not detect any significant line emitter within the FoVs. This result holds if we decrease the detection threshold to 4.5σ, which is roughly consistent with the negative tail of the S/N distributions of our cubes. Note that Venemans et al. (2016) also reported a non-detection of other line emitters within the ALMA band 6 FoVs of three luminous $z > 6$ VIKING quasars. Regarding luminous [C II] emitters ($L_{\rm [C\,II]} \gtrsim 10^9\,L_\odot$), our non-detection is broadly consistent with Decarli et al. (2017) as well, who reported four companion luminous [C II] emitting galaxies out of 25 luminous quasar fields at $z \gtrsim 6$: based on their detection rate (16%), the expected number of such luminous [C II] emitters for our observations is at most one. Furthermore, Trakhtenbrot et al. (2017) reported three detections of associated luminous SMGs ($L_{\rm [C\,II]} \gtrsim 10^9\,L_\odot$) out of six luminous quasar fields at $z \simeq 4.8$, implying a higher merger frequency at that redshift than at $z \sim 6$. Compared to those observations (Decarli et al. 2017; Trakhtenbrot et al. 2017), our observations are much deeper. Therefore, the non-detection of [C II] emitters in our fields would place a more stringent constraint on a [C II] luminosity function at that redshift, which is beyond the scope of this paper.

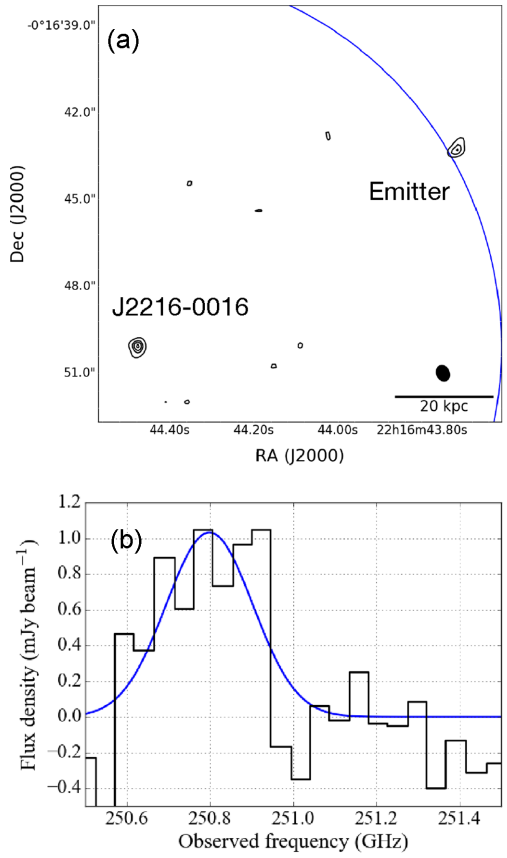

Fig. 4. (a) A line emitter found in the J2216−0016 field that is 13.″2 away from the quasar. The curve indicates the nominal field of view (∼12″ radius) of this ALMA band 6 observation. The contours step as 3σ, 5σ, 6σ, and 7σ (1σ = 13.2 μJy beam^{-1}). The synthesized beam is plotted in the bottom right-hand corner. (b) The observed spectrum of the line emitter shown in (a), with the single-Gaussian fit superposed. See text for the result of the fit. (Color online)

3.4.2 Continuum emitters

With the rms values listed in table 1, we conservatively considered sources with a signal-to-noise ratio (S/N) $\geq$5 as continuum emitters. In the fields of J0859+0022 (5σ = 48 μJy beam^{-1}), J1152+0055 (104 μJy beam^{-1}), and J1202−0057 (44 μJy beam^{-1}), no significant emitter was found. In contrast, one emitter *candidate* was found slightly outside the nominal FoV of J2216−0016 (5σ = 66 μJy beam^{-1}; figure 4a), 13.″2 away from the quasar. Its coordinates are RA = 22$^{\rm h}$16$^{\rm m}$43.$^{\rm s}$718, Dec = −00°16′43.″28.

However, this source turned out to be a line emitter, after a careful inspection of all spectral windows (figure 4b), rather than a continuum emitter. That is, this source is not detected in the continuum map of J2216−0016 after the channels with faint line emission were removed. A single-Gaussian fit to the line gave an amplitude, centroid, and integrated intensity of 1.03 ± 0.09 mJy, 250.80 ± 0.01 GHz, and 0.32 ± 0.03 Jy km s^{-1}, respectively. We suggest that the source is a lower-redshift object, as it is detected

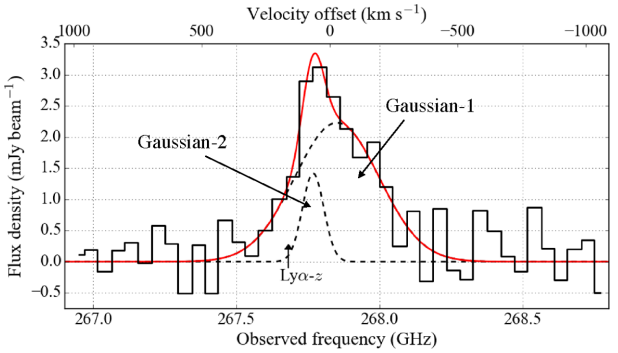

Fig. 5. A double-Gaussian fit to the [C II] spectrum of J2216−0016 (red solid line), with the black dashed lines indicating each component. The upper axis denotes the velocity offset from the centroid of the single-Gaussian profile shown in figure 2. The expected [C II] frequency from the Lyα-based redshift is also indicated. (Color online)

in all of the HSC bands as $g = 26.90 \pm 0.26$ mag, $r = 25.59 \pm 0.18$ mag, $i = 24.59 \pm 0.06$ mag, $z = 23.82 \pm 0.09$ mag, and $y = 23.10 \pm 0.06$ mag, which is typically not the case for high-redshift galaxies. Indeed, the HSC photometric-redshift catalog from the first data release (with the Mizuki-code, Tanaka 2015; Tanaka et al. 2017) suggests that the source is at $z_{\rm photo} = 1.32 \pm 0.11$. In this case, the line could be CO(5–4) emission [expected redshift $z_{\rm CO(5\text{-}4)} = 1.298 \pm 0.003$].

In short, we did not find any significant continuum emitter in these four fields (each has $\simeq$ 0.135 arcmin^2 field of view; ∼0.54 arcmin^2 total) even at our high sensitivities (5σ = 44–104 μJy beam^{-1}). It is noteworthy, on the other hand, that many studies suggest that luminous quasars tend to reside in over-dense region of continuum emitters (e.g., Silva et al. 2015, and references therein): our result of the lower luminosity quasars at $z \gtrsim 6$ seems not to match those findings. Further studies on, e.g., halo masses of those less-luminous quasars, are needed to reveal underlying physical differences between the environments of various kinds of quasars.

The non-detection in the four fields seems to be lower than would be expected from recent 1.2 mm number counts (e.g., Aravena et al. 2016; Fujimoto et al. 2016). For example, the cumulative number count in Fujimoto et al. (2016) is ∼8 (total number) in our four fields (∼2–3 in each 0.135 arcmin^2 field), whilst no source was detected. However, the discrepancy in each field is still statistically not so significant (∼1σ–2σ; Gehrels 1986): we would also suggest several possible factors that can further reconcile the discrepancy. One factor is cosmic variance, given the small area we probed. A low selection-completeness expected for high-resolution (e.g., ∼0.″5) observations (see figure 5 in Fujimoto et al. 2017) will reduce the detection rate. It is also possible that previous counts using low-significance detections are contaminated by noise components, as suggested

by Oteo et al. (2016) and Umehata et al. (2017). *Pseudo continuum emitters*, which we found in the J2216−0016 field (figure 4), could also be contaminants, particularly at the faint end. The accumulation of datasets of individually very deep observations will help to further constrain the true mm/submm number count at the faint end ($\lesssim 100\,\mu$Jy): this will be investigated with our growing SHELLQs sample.

3.5 Any peculiarity in the BAL quasar J2216−0016?

Among the four HSC quasars studied here, J2216−0016 shows a clear broad absorption line (BAL) feature (e.g., Weymann et al. 1991; Trump et al. 2006) in its N V spectrum (Matsuoka et al. 2016). As the BAL feature is a clear manifestation of nuclear outflows, which could be an indication of AGN-feedback on the host galaxy, it is interesting to see if there is any peculiarity in the host galaxy. Indeed, the relatively large spatial extent of the [C II] emitting region (5.2 ± 0.8 kpc; table 3) as well as the high $\mathrm{EW}_{[\mathrm{C\,II}]}$ ($4.08 \pm 0.87\,\mu$m, compared to the value of $\simeq 1.0\,\mu$m for local starburst galaxies; Sargsyan et al. 2014) already stands out among the four HSC quasars.

As an initial investigation, we fit the observed [C II] spectrum with a double-Gaussian profile (figure 5): the resultant reduced χ^2 is 1.05 (degree of freedom, d.o.f. = 14), which is improved over the single-Gaussian fit (reduced $\chi^2 = 1.24$ with d.o.f = 17).[6] The two double-Gaussian constituents have centroid frequencies of 267.851 GHz (Gaussian-1) and 267.768 GHz (Gaussian-2), respectively. The Gaussian-2 has a much narrower FWHM (99.1 km s^{-1}) than the Gaussian-1 (389.7 km s^{-1}) has. It is therefore plausible that the Gaussian-1 component corresponds to the quasar host, once we take into account the [C II] FWHM of the quasar host galaxies studied so far. Figure 6 shows the integrated intensity of the [C II] emission divided into the redder and bluer velocity components. The redder component that contains the Gaussian-2 is spatially more extended than the bluer one, towards the north to northeast direction. That elongation has a different position angle (P.A.) of $\sim 15^\circ$ from the bluer component, and most of the redder component around the continuum peak (P.A. $\sim -25^\circ$ to -40°), implying that the elongation traces a physically different structure from the quasar host galaxy.

One plausible origin for the elongated structure is an AGN-driven [C II] outflow, such as that observed in the luminous $z = 6.42$ quasar SDSS J1148+5251 (Maiolino et al. 2012; Cicone et al. 2015). In this case, the decomposed line profile suggests that the outflow is single-sided relative to the systemic velocity of the quasar host, although its width is rather narrow as compared to previously observed [C II] outflows. Similar single-sided outflows have been observed in many systems (e.g., Cicone et al. 2014; Feruglio et al. 2017). Note that the blueshifted BAL absorption feature does not necessarily preclude the existence of redshifted outflows.

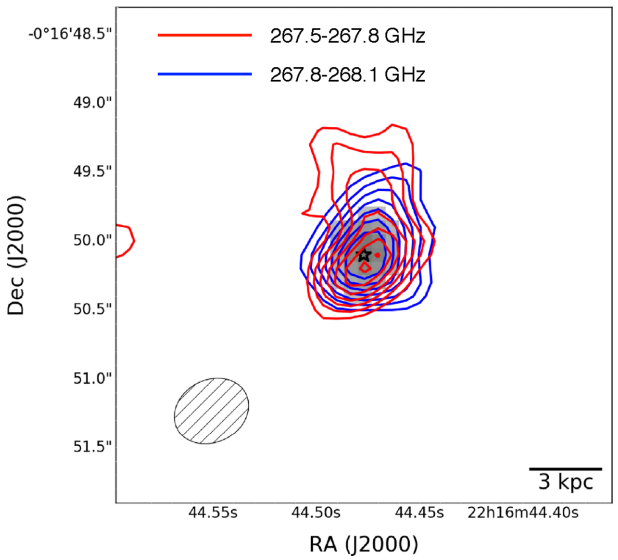

Fig. 6. The integrated [C II] line emission (moment 0) map of J2216−0016 divided into the redder half (red contours, containing the Gaussian-2; 267.5–267.8 GHz) and the bluer half (blue contours, containing the Gaussian-1; 267.8–268.1 GHz), overlaid on the continuum map (grayscale; figure 1). The contours step as 3σ, 4σ, 5σ, ..., 8σ, and 9σ, with $1\sigma = 0.023$ Jy beam^{-1} km s^{-1}. There is no significant offset between the peaks. The central star marks the peak location of the rest-FIR continuum emission. The synthesized beam is shown in the bottom left-hand corner. (Color online)

Another plausible origin of the offset is a galaxy merging with the quasar host with a projected separation of $\lesssim 5$ kpc. High resolution and deep optical/infrared imaging data, which is not available at this moment, will give a crucial hint on the nature of the extended component. A similarly close (projected distance $\sim$5 kpc) galaxy was also found near the moderate-luminosity ($M_{1450} = -25.6$) quasar PSO J167-13 (Willott et al. 2017), which demonstrates the importance of high angular resolution in unveiling such close companion(s). If we suppose that the merging system has the same spatial extent as the quasar host itself, the much narrower FWHM roughly translates to a dynamical mass that is an order of magnitude smaller, i.e., this event will be a minor merger, which would enhance nuclear activity (e.g., Taniguchi 1999; Kaviraj 2014). Such an evolutionary link between the BAL and early galaxy evolution is an appealing topic for further investigation (e.g., Farrah et al. 2007).

In either case, we clearly need higher resolution and sensitivity to isolate the candidate structure spatially and to distinguish between these two scenarios, particularly via

[6] We evaluated the fit within the frequency range of 267.41–268.30 GHz.

studying the gas dynamics. In what follows, we use dynamical properties from the single-Gaussian fit.

4 Discussion

In this section, we first explore the star-forming nature of the HSC quasar host galaxies, and then discuss the early co-evolutionary relationship at $z \sim 6$, paying attention to the physical differences between optically-luminous ($M_{1450} \lesssim -26$) and low-luminosity ($M_{1450} \gtrsim -25$) quasars. We will also compare the observed properties with theoretical predictions from semi-analytic models, particularly those from a *new numerical galaxy catalog* (ν^2GC; Makiya et al. 2016). In this catalog, the underlying merging histories of dark matter haloes are based on state-of-the-art cosmological N-body simulations (Ishiyama et al. 2015), which have high mass resolution and quite large volumes relative to previous simulations, which are particularly suitable to study statistical properties of rare populations such as massive/luminous quasars at high redshifts (Shirakata et al. 2018). The ν^2GC simulation uses prescriptions for star formation, gas heating by UV feedback, supernova feedback, SMBH growth, and AGN feedback (see also Enoki et al. 2014; Shirakata et al. 2015), to trace galaxy evolution. In this study, we adopt the results from a subset of the ν^2GC with the largest volume, i.e., ν^2GC-L (Ishiyama et al. 2015), for which the box size is $1.12\,h^{-1}$ comoving Gpc and the dark-matter mass resolution is $2.20 \times 10^8\,h^{-1}\,M_\odot$ (number of particles $= 8192^3$).

4.1 The [C II]-FIR luminosity relation

The [C II]/FIR luminosity ratio can reflect physical conditions in the star-forming clouds. It has long been known that this ratio is more than an order of magnitude smaller in sources with high $L_{\rm FIR}$ than low (e.g., Malhotra et al. 1997; Luhman et al. 2003; Brauher et al. 2008; Stacey et al. 2010; Graciá-Carpio et al. 2011; Díaz-Santos et al. 2013). This trend has also been extensively studied in the high-redshift universe (e.g., Carilli & Walter 2013). Possible causes of the *[C II]-deficit in FIR-luminous objects* include AGN contamination of $L_{\rm FIR}$ (Sargsyan et al. 2014), reduction of C^+ abundance due to AGN-heating (Langer & Pineda 2015), charging of dust grains (Malhotra et al. 1997), saturation of the line flux due to high gas density (Kaufman et al. 1999), high dust opacity with respect to gas in dust-bounded regions due to an increase of the average ionization parameter (Abel et al. 2009; Graciá-Carpio et al. 2011), and high gas surface density of individual clouds (or higher molecular-to-atomic gas fraction, Narayanan & Krumholz 2017).

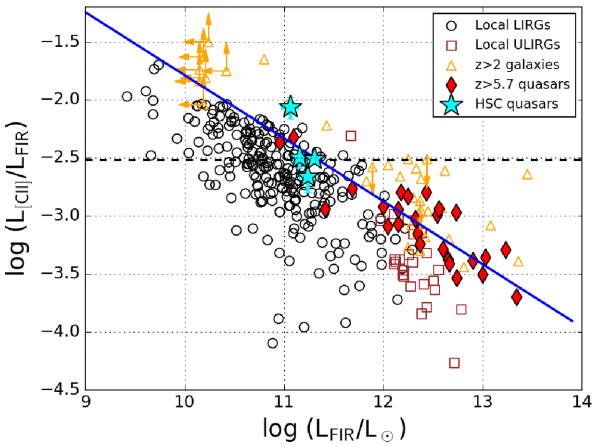

Fig. 7. [C II]/FIR luminosity ratio as a function of FIR luminosity for our HSC quasars (cyan stars). Also plotted are compilations of various kinds of galaxies from the recent literature for a comparison: local LIRGs (Díaz-Santos et al. 2013), local ULIRGs (Farrah et al. 2013), $z > 2$ star-forming galaxies (mostly FIR-selected SMGs, plus some UV-selected galaxies, Maiolino et al. 2009; Ivison et al. 2010; De Breuck et al. 2011; Wagg et al. 2012; Riechers et al. 2013; Gullberg et al. 2015; Capak et al. 2015), and $z > 5.7$ quasars (Maiolino et al. 2005; Wang et al. 2013, 2016; Willott et al. 2013, 2015, 2017; Bañados et al. 2015; Venemans et al. 2012, 2016, 2017; Decarli et al. 2017, 2018; Mazzucchelli et al. 2017). The dashed horizontal line indicates the Milky Way value as a reference ($\sim 3 \times 10^{-3}$, Carilli & Walter 2013). Where necessary, TIR (8–1000 μm) measurements were converted to FIR luminosity using $L_{\rm TIR} \simeq 1.3\,L_{\rm FIR}$ (Carilli & Walter 2013). The diagonal solid blue line indicates our best fit to the $z > 5.7$ quasars. Errors are only indicated for the HSC quasars to enhance the clarity of the figure. (Color online)

Figure 7 shows this [C II]-deficit in the FIR-luminous regime with a compilation of galaxies in both the nearby and high-redshift universes, including $z \gtrsim 6$ quasars. Those quasars also show a deficit with increasing $L_{\rm FIR}$ (e.g., Venemans et al. 2016; Wang et al. 2013). However, the HSC quasars, as well as other less-luminous quasars (i.e., CFHQS quasars, Willott et al. 2013, 2015, 2017), exhibit $L_{\rm [C\,II]}/L_{\rm FIR}$ ratios comparable to or slightly higher than the local LIRG-class objects at fixed $L_{\rm FIR}$ (Díaz-Santos et al. 2013).[7] In terms of $\rm EW_{[C\,II]}$, we also found that the HSC quasars have comparable values to local star-forming galaxies in table 2, while the luminous-end quasars tend to show lower $\rm EW_{[C\,II]}$ (Venemans et al. 2016).

The physical origin of the difference in $L_{\rm [C\,II]}/L_{\rm FIR}$ between those optically-luminous and -faint quasars is thus of interest. Both a higher AGN contribution to $L_{\rm FIR}$ and reduction of C^+ abundance due to too-strong X-ray irradiation can reduce the ratio in luminous-end AGNs (Sargsyan et al. 2014; Langer & Pineda 2015). As the spatial extent of [C II] or FIR continuum-emitting regions are comparable between the HSC quasars and optically-luminous quasars

[7] We use $L_{\rm FIR}$ ($T_{\rm d} = 35$ K) in table 2 as this case yields better agreement with [C II]-based SFR than that of $T_{\rm d} = 47$ K. The same $T_{\rm d}$ is assigned for J2216−0016 as well to keep consistency, although its SFR with $T_{\rm d} = 47$ K agrees better with that derived from the [C II] luminosity.

(see table 3), a higher charge on dust grains due to enhanced star-forming activity (Malhotra et al. 1997) and higher gas surface density that shields ionizing radiation or cosmic rays could also cause the discrepancy (Narayanan & Krumholz 2017).

High-redshift quasars follow a correlation in this plane that has a comparable slope to the relation seen for lower-redshift objects, but is offset in the higher $L_{[\mathrm{C\,II}]}/L_{\mathrm{FIR}}$ direction. We fitted the relationship for the high-redshift quasar sample including the objects in this study following Willott et al. (2017). The orthogonal distance regression gives

$$\log_{10} L_{[\mathrm{C\,II}]}/L_{\mathrm{FIR}} = (3.84 \pm 0.57) - (0.56 \pm 0.05) \log_{10} L_{\mathrm{FIR}}, \quad (1)$$

which is consistent with the relation derived in Willott et al. (2017). This relation is offset from the trend for the local galaxies and U/LIRGs by a factor of ∼2–3 in the sense that $L_{[\mathrm{C\,II}]}/L_{\mathrm{FIR}}$ is higher for the quasars. It is also noteworthy that high-redshift, FIR-luminous star-forming galaxies (i.e., non-AGN objects) also show an offset from the local trend (e.g., Maiolino et al. 2009). Thus, this trend is characteristic of high-redshift, FIR-luminous objects regardless of the nature of their nuclear heating source(s). This could be due to the fact that those objects have more available gas (Narayanan & Krumholz 2017): at a fixed L_{FIR} or SFR, higher gas mass can translate to lower gas mass *surface* density of an individual cloud (linked to a star formation efficiency), which reduces the ability of shielding ionizing photons and cosmic rays. In that case, we would expect a higher [C II]/CO abundance ratio, as the column density for shielding ionizing photons and cosmic rays decreases there (low surface density). However, a more thorough study of the true shape of the FIR spectra of high-redshift objects is necessary to constrain $L_{[\mathrm{C\,II}]}/L_{\mathrm{FIR}}$ ratios accurately and to infer the physical properties of the gas content (e.g., Stacey et al. 2010) in the early universe.

4.2 Cold dust content

The rapid enrichment of the ISM at the $z \gtrsim 6$ universe, which is reflected in the large amounts of cold dust in quasar hosts (e.g., several $\times 10^8\,M_\odot$ in SDSS quasars, Wang et al. 2008, 2011a), has been a challenge for many theoretical studies (Valiante et al. 2017, for a recent review). Similar high (or even higher) M_{dust} values have also been observed in SMGs at $z > 6$ (Riechers et al. 2013; Strandet et al. 2017). Recent models particularly stress the importance of grain growth in cold, dense gas clouds, rather than stellar yields, as the dominant source of the early dust production (e.g., Michałowski et al. 2010; Mancini et al. 2015; Popping et al. 2017). In these models, the observed M_{dust} of both optically/FIR-luminous quasars (e.g., SDSS) and faint HSC quasars (several $\times 10^7\,M_\odot$; table 2) can be reproduced by modifying the characteristic dust accretion time scale (τ_{acc}, e.g., Hirashita & Voshchinnikov 2014).

According to the latest dust evolution model of Popping, Somerville, and Galametz (2017), which also incorporates several other dust formation and destruction processes, a $\tau_{\mathrm{acc}} \sim 15$ Myr model can yield $M_{\mathrm{dust}} \sim$ several $\times\ 10^8\,M_\odot$ in a galaxy with a stellar mass (M_*) of several $\times\ 10^{10}\,M_\odot$ at $z \sim 6$. Meanwhile, decelerated dust growth with $\tau_{\mathrm{acc}} \sim 100$ Myr is sufficient to produce $M_{\mathrm{dust}} \sim$ several $\times\ 10^7\,M_\odot$ in a similar M_* galaxy. This M_* would be valid for the $z \gtrsim 6$ quasar hosts observed so far at the rest-FIR, as long as their dynamical masses (subsection 4.3) mostly reflect their M_*. As this timescale depends on the molecular gas density of the system (n_{H2}) as $\tau_{\mathrm{acc}} \propto n_{\mathrm{H2}}^{-1}$, the possible factor of ∼10 difference in gas mass surface density between optically-luminous quasars and the HSC quasars at $z \gtrsim 6$ (subsection 3.3) can explain the difference in τ_{acc} as well. Note that τ_{acc} also depends on the inverse of the gas phase metallicity. Thus, if the difference in M_{dust} is eventually attributable to the difference in n_{H2}, we expect that the gas-phase metallicity of optically-luminous and -faint systems will not differ markedly. On the other hand, if n_{H2} is somehow comparable between them, the less-luminous HSC quasars would have ∼1/10 the gas metallicity, as would the luminous-end quasars. This can be tested by a multi-species excitation analysis (e.g., Wang et al. 2016) or by metallicity measurements that combine multiple fine-structure lines (e.g., Nagao et al. 2012).

4.3 Star-forming activity

The majority of star-forming galaxies are found to populate the so-called *main sequence* (MS) of star formation on the M_*–SFR plane (e.g., Daddi et al. 2007; Elbaz et al. 2007), and the evolution of the MS over cosmic time has been studied extensively, even up to $z \sim$ 5–6 (Speagle et al. 2014; Steinhardt et al. 2014; Tasca et al. 2015; Salmon et al. 2015). The MS can be used to define starburst galaxies, normal star-forming galaxies, and quenched/quiescent galaxies at each redshift. While the MS is not well constrained at $z \gtrsim 5$, it is still informative to place $z \gtrsim 6$ quasars on the M_* vs. SFR plane and compare the levels of star formation among other galaxies.

To this end, we first computed dynamical masses (M_{dyn}) of the HSC quasars by following the standard procedure in previous $z \gtrsim 6$ quasar studies (e.g., Wang et al. 2010, 2013; Willott et al. 2015; Venemans et al. 2016): here, we assumed that the observed [C II] emission came from a thin disk such that the velocity structure reflects rotational motion. The inclination angle of the disk (i) is

determined by the ratio of the deconvolved (table 3) major ($a_{\rm maj}$) and minor ($a_{\rm min}$) axes of the [C II] emitting regions, $i = \cos^{-1}(a_{\rm min}/a_{\rm maj})$. The circular velocity ($v_{\rm circ}$) is calculated as $v_{\rm circ} = 0.75\,{\rm FWHM}_{\rm [C\,II]}/\sin i$ (Wang et al. 2010): the ${\rm FWHM}_{\rm [C\,II]}$ values of the HSC quasars are listed in table 2. The disk size (diameter, D) is approximated as $D = 1.5 \times a_{\rm maj}$ to account for the spatially extended component (i.e., full width at 20% of the peak intensity for a Gaussian profile) to maintain consistency with the previous works shown above.

Then, the $M_{\rm dyn}$ enclosed within D is given by

$$M_{\rm dyn}/M_\odot = 1.16 \times 10^5 \left(\frac{v_{\rm circ}}{\rm km\,s^{-1}}\right)^2 \left(\frac{D}{\rm kpc}\right) \quad (2)$$

The resultant values are listed in table 4. Note that the errors on $M_{\rm dyn}\sin^2 i$ are estimated from the ${\rm FWHM}_{\rm [C\,II]}$ and source size. On the other hand, formal errors on $M_{\rm dyn}$ themselves (i.e., after correcting for the inclination angles) are not given due to multiple uncertainties including those of the inclination angles and the true geometry of the line-emitting regions.

Keeping the existence of such a large *unconstrained* systematic uncertainty in mind, hereafter we use the above $M_{\rm dyn}$ as a surrogate for M_*, which is a common procedure in high-redshift quasar studies (e.g., Wang et al. 2010, 2013; Willott et al. 2015, 2017; Venemans et al. 2016). Note that in three of our HSC quasars, gas masses obtained by applying a plausible gas-to-dust mass ratio (e.g., 100, Draine et al. 2007) to our derived $M_{\rm dust}$ are small relative to $M_{\rm dyn}$, indicating that stellar components dominate their $M_{\rm dyn}$. The one exception is J1152+0055, the inferred gas mass of which is ∼50% of $M_{\rm dyn}$, but this still has a limited impact on our conclusions. The resultant M_* values clearly constitute the massive end of $z \sim 6$ galaxies (e.g., Grazian et al. 2015).

The relationship between M_* and SFR (calculated with $L_{\rm FIR}$) of the HSC quasars is plotted in figure 8, along with $z \sim 6$ results from the ν^2GC simulation: the simulated M_* values (not $M_{\rm dyn}$) are used here. We selected $\simeq 41000$ galaxies hosting $\geq 10^7\,M_\odot$ SMBHs from the simulated catalog (see also subsection 4.4), all of which are indeed high-M_* galaxies. The simulated galaxies show two sequences, a starburst sequence (upper) and MS (lower): the gap between these two sequences is artificial due to the limited mass- and time-resolution of the model (see details in Shirakata et al. 2018).[8]

Keeping this in mind, the simulated galaxies are used to infer the star-formation levels of the observed quasars. The model-MS is consistent with other semi-analytic models

[8] We confirmed that this effect has little impact on time-integrated quantities such as $M_{\rm dyn}$, M_*, and $M_{\rm BH}$, which are used in subsection 4.4.

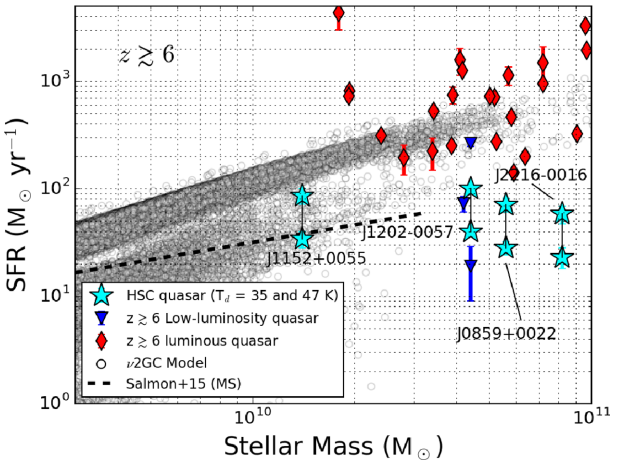

Fig. 8. $\rm SFR_{TIR}$ as a function of M_* for the HSC quasars (cyan stars), the $z \gtrsim 6$ luminous ($M_{1450} \lesssim -26$; red diamonds) and the $z \gtrsim 6$ low-luminosity ($M_{1450} > -25$; blue triangles) quasars with $10^{10} \leq M_{\rm dyn}/M_\odot \leq 10^{11}$. For the HSC quasars, we show both cases of $T_{\rm d} = 35$ K and 47 K, to exhibit the level of uncertainty due to unconstrained $T_{\rm d}$. Those $M_{\rm dyn}$ are used as surrogates for M_* in this plot. Background circles show simulated $z \sim 6$ galaxies hosting $M_{\rm BH} \geq 10^7\,M_\odot$ SMBHs from the ν^2GC model. Two sequences, namely the starburst-sequence and the star-forming main-sequence (MS), are apparent in the model. The latter is consistent with the recently suggested MS at $z \sim 6$ from rest-frame UV-to-NIR photometric observations (Salmon et al. 2015, black dashed line). (Color online)

(e.g., Somerville et al. 2008), and roughly matches the recently *observed* MS at $z \sim 6$ (investigated at $M_* \lesssim 10^{10.5}\,M_\odot$, Salmon et al. 2015). At lower-z, the model is also consistent with observations (e.g., Daddi et al. 2007; Elbaz et al. 2007). As seen in figure 8, the HSC quasars studied here all reside *on* or even *below* the MS at $z \sim 6$, compared to both the ν^2GC model and the observed relationship. Therefore, we suggest that these HSC quasars are now ceasing their star-forming activities, and are transforming into the quiescent population.

We also plot $z \gtrsim 6$ optically-luminous ($M_{1450} \lesssim -26$) and low-luminosity ($M_{1450} > -25$) quasars with [C II] observations (Maiolino et al. 2005; Venemans et al. 2012, 2016; Wang et al. 2013, 2016; Bañados et al. 2015; Willott et al. 2015, 2017; Decarli et al. 2017, 2018; Mazzucchelli et al. 2017) in figure 8. Here, we limit the sample to have $10^{10} \leq M_{\rm dyn}/M_\odot \leq 10^{11}$ for fair comparison with the HSC quasars, after considering a recent argument that both the SFR and mass accretion rate may depend on the M_* of the host galaxy (Yang et al. 2017). Again, their $M_{\rm dyn}$ values are used as surrogates for M_*.

We found that these optically-luminous quasars all reside *on* or *above* the MS, i.e., their hosts are indeed starburst galaxies. On the other hand, two of the three (optically) low-luminosity quasars (CFHQS quasars; Willott et al. 2015, 2017) which have comparable M_{1450} to our HSC quasars also exhibit similarly low SFRs. Therefore,

Table 4. Dynamical properties of the HSC quasars.*

Name	$M_{\rm dyn}\sin^2 i$ ($10^{10}\,M_\odot$)	$M_{\rm dyn}$ ($10^{10}\,M_\odot$)	$M_{\rm BH}$ ($10^8\,M_\odot$)
J0859+0022	3.3 ± 1.1	5.6	$0.2^{+0.2}_{-0.1}$
J1152+0055	1.1 ± 0.5	1.4	$4.3^{+7.8}_{-2.8}$
J2216−0016	6.4 ± 1.3	8.2	$6.1^{+6.1}_{-3.0}$
J1202−0057	2.9 ± 0.8	4.4	$0.4^{+0.7}_{-0.3}$

*Formal errors on $M_{\rm dyn}$ are not given due to multiple unconstrained uncertainties including those of the inclination angles and the geometry of the line-emitting regions. See details about the $M_{\rm BH}$ measurement of J0859+0022 and J2216−0016 with the Mg II-based calibrations (Vestergaard & Osmer 2009) in M. Onoue et al. (in preparation). For the remaining two quasars, Eddington-limited mass accretion is assumed, which gives the lower limit on $M_{\rm BH}$. A typical uncertainty is 0.3 dex for the Mg II-based $M_{\rm BH}$ (Shen et al. 2008), and 0.45 dex for the Eddington ratio-based $M_{\rm BH}$ (Willott et al. 2015), respectively.

host galaxies of those optically-luminous quasars and less-luminous quasars, including our HSC quasars, plotted in figure 8 constitute different populations in terms of the evolutionary stages of star formation. The order of magnitude difference in gas mass surface density implied in this work could drive the above difference in both SFR and mass accretion rate (e.g., Hopkins & Quataert 2010). We also point out that a gap between the luminous quasars and the HSC quasars stands out. A transformation from the starburst phase to the quiescent phase would thus be quite rapid: merger-induced galaxy evolution models, for example, indeed predict such evolution (e.g., Hopkins et al. 2008; Volonteri et al. 2015).

Note that, however, those FIR luminous quasars could only be a subset of all optically-luminous quasars at $z \gtrsim 6$, according to the compilation in Calura et al. (2014), as the majority of the quasars reported there only have upper limits on $L_{\rm FIR}$ (mostly measured with single-dish observations). The reported upper limits in Calura et al. (2014) are typically $\sim(3\text{–}6) \times 10^{12}\,L_\odot$. Thus, it is plausible that a large number of optically-luminous quasars could lie on the MS, which makes the actual fraction of $z \gtrsim 6$ luminous quasars that are hosted by starburst galaxies highly uncertain. Meanwhile, the recent ALMA survey toward $z \gtrsim 6$ optically-luminous quasars, without prior information on their FIR fluxes, revealed that the bulk of them indeed have ULIRG-like $L_{\rm FIR}$ (Decarli et al. 2018). It is therefore also possible that the $z \gtrsim 6$ quasars compiled in Calura et al. (2014) actually have ULIRG-like (or luminous LIRG-like) $L_{\rm FIR}$, which are yet below the detection limits of previous single-dish observations. Deeper submm observations are clearly required to depict the true quasar distribution on the M_*–SFR plane.

It is also noteworthy that the spatial extents (both [C II] and continuum) of the HSC quasars are consistent with the typical size of the stellar components of some compact quiescent galaxies (cQGs, e.g., van Dokkum et al. 2008; Krogager et al. 2014) exhibiting little ongoing star formation. Such cQGs have been found even at $z \sim 4$ (Straatman et al. 2014, 2015). Multi-band photometric analysis (Straatman et al. 2014) suggests that the stellar mass of $z \sim 4$ cQGs (several $\times\, 10^{10}\,M_\odot$) had been formed at $z \sim 6$ with intense starburst (characteristic time scale $\sim$100 Myr). Within the context of this scenario, the host galaxies of HSC quasars at $z \sim 6$ may represent an earlier phase in the formation of massive compact galaxies, possible through mergers, when star formation is beginning its cessation. Indeed, recent studies on the sizes and star formation histories of submillimeter galaxies (SMGs) and cQGs suggest that cQGs are descendants of SMGs at higher redshifts, having passed through the optical quasar phase, which will further evolve into local giant ellipticals through dry mergers (e.g., Toft et al. 2014; Ikarashi et al. 2015; Fujimoto et al. 2017).

4.4 Early SMBH-host galaxy co-evolution in the less-luminous quasars

Finally, we investigate the nature of the early co-evolution of SMBHs and their hosts. To this end, we compute $M_{\rm BH}$ for the HSC quasars (table 4). For J0859+0022 and J2216−0016, a virial calibration using broad Mg II emission line (Vestergaard & Osmer 2009) was applied to derive their $M_{\rm BH}$ (M. Onoue et al. in preparation). It is noteworthy that J0859+0022 has a very low $M_{\rm BH}$ ($\sim 2 \times 10^7\,M_\odot$) compared to previously-known $z \gtrsim 6$ quasars, clearly demonstrating the high sensitivity of our HSC survey in discovering such lower-mass objects. For the remaining two cases, the Eddington-limited mass accretion was assumed, following previous $z \gtrsim 6$ quasar studies (e.g., Wang et al. 2013; Venemans et al. 2016), which gives the lower-limit on $M_{\rm BH}$. Their bolometric luminosities were calculated from the rest-frame UV luminosity at 1450 Å with a correction factor of 4.4 (Richards et al. 2006). The $M_{\rm dyn}$ values derived in subsection 4.3 are again used here as surrogates for M_*.

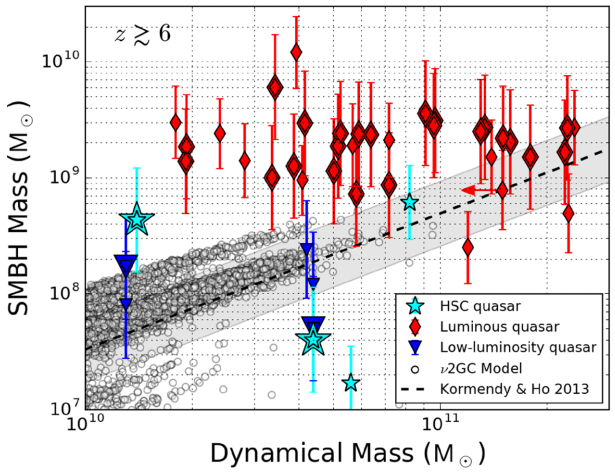

Fig. 9. $M_{\rm BH}$ vs. host galaxy $M_{\rm dyn}$ for $z \gtrsim 6$ quasars. The HSC quasars (cyan stars) are shown along with ν^2GC model predictions at $z \sim 6$ (white circles). The diagonal dashed line indicates the local $M_{\rm BH}$–$M_{\rm bulge}$ relationship with its intrinsic scatter in the shaded region (Kormendy & Ho 2013). We equate $M_{\rm dyn}$ and $M_{\rm bulge}$ in this plot. Also shown are $z \gtrsim 6$ optically-luminous ($M_{1450} \lesssim -26$) quasars (red diamonds) and less-luminous ($M_{1450} > -25$; similar to the HSC quasars) ones (blue triangles). The less-luminous quasars, including the HSC ones, lie close to the local relation, whereas the luminous quasars show departures particularly at $M_{\rm dyn} < 10^{11}\,M_\odot$. Among the four HSC quasars, Mg II-based $M_{\rm BH}$ is available for J0859+0022 and J2216−0016, whereas the Eddington-limited accretion is assumed for the rest (see table 4). The double symbols indicate that the Eddington-limited accretion is assumed to derive their $M_{\rm BH}$. (Color online)

We have also compiled $M_{\rm BH}$ or M_{1450} (Willott et al. 2003, 2010b; De Rosa et al. 2014; Venemans et al. 2015a, 2015b; Kashikawa et al. 2015; Wu et al. 2015; Bañados et al. 2016, 2018; Jiang et al. 2016; Shao et al. 2017; Mazzucchelli et al. 2017; Decarli et al. 2018) and [C II]-based $M_{\rm dyn}$ (Maiolino et al. 2005; Venemans et al. 2012, 2016, 2017; Wang et al. 2013, 2016; Bañados et al. 2015; Willott et al. 2015, 2017; Decarli et al. 2017, 2018; Mazzucchelli et al. 2017) measurements for $z \gtrsim 6$ quasars from the literature. The $M_{\rm BH}$ estimates are based on Mg II measurements with a typical uncertainty of 0.3 dex (Shen et al. 2008), which is added in quadrature to their measurement uncertainties. We assumed Eddington-limited accretion for those objects without Mg II data after deriving their bolometric luminosities from M_{1450}: 0.45 dex uncertainty is assumed for those $M_{\rm BH}$ (Wang et al. 2013; Willott et al. 2015). While this provides a lower limit to their $M_{\rm BH}$, this assumption would be reasonable since optically-luminous $z \gtrsim 6$ quasars are known to radiate closely at the Eddington limit (e.g., Willott et al. 2010b). Following the procedure of Willott et al. (2017), we assigned $D = 4.5$ kpc and a random orientation angle $i = 55^\circ$ to some unresolved host galaxies in order to estimate their average sizes.

All of the above-mentioned quasars are plotted in figure 9, overlaid with the local $M_{\rm BH}$–$M_{\rm bulge}$ relation (Kormendy & Ho 2013). The $M_{\rm dyn}$ of the central few kpc regions of high-redshift quasars can be equivalent to local $M_{\rm bulge}$ in the absence of further gas accretion and/or mergers. Thus, it is instructive to place the high-redshift quasars on this plane. As selection bias favoring the most luminous objects (or most massive objects) would have distorted the shape of the early co-evolutionary relations studied previously (section 1), we further divide the literature sample into (i) optically-luminous objects ($M_{1450} < -25$; mostly <-26) and (ii) less-luminous objects ($M_{1450} > -25$), based on the compiled quasar and galaxy luminosity functions at $z \sim 6$ in Matsuoka et al. (2016).

Figure 9 confirms the previous argument of Willott et al. (2017) that there is no clear correlation between the two quantities when we focus on the all $z \gtrsim 6$ quasars observed so far, and the scatter is much larger than the local relation, particularly at $M_{\rm dyn} < 10^{11}\,M_\odot$. At least in this galaxy mass range, the underlying $M_{\rm BH}$ distribution would have a wide scatter, and thus observations can be biased toward more luminous or more massive objects (e.g., Lauer et al. 2007; Schulze & Wisotzki 2014). This is demonstrated by the different distributions of the optically-luminous (e.g., SDSS quasars) and less-luminous (including HSC) quasar populations: the luminous quasars clearly have over-massive SMBHs compared to the local relation in this mass range, whereas less-luminous quasars are roughly consistent with the local relation within their uncertainties. We now see this difference more clearly than previous studies, since we almost double the number of low-luminosity quasars with $M_{\rm dyn}$ measurements in this study. Therefore, our study highlights the importance of probing low-luminosity quasars to understand the unbiased early co-evolutionary relation reflecting the bulk of the AGN-host galaxies in this epoch, although the sample is still too small to claim this argument statistically.

We also compare the observed distributions of $z \sim 6$ quasars on the plane with simulated galaxies from the ν^2GC model, which are also plotted in figure 9. Here, we selected all galaxies containing $M_{\rm BH} \geq 10^7\,M_\odot$ SMBHs at $z \sim 6$ as we focused on massive quasars. The simulation traces the SMBH growth from the seed mass of $10^3\,M_\odot$.[9] The galaxy bulge and the central SMBH gain mass, while maintaining the relation (Makiya et al. 2016),

$$\Delta M_{\rm BH} = f_{\rm BH} \Delta M_{*,\rm burst}, \tag{3}$$

where $\Delta M_{*,\rm burst}$ is the total mass of stars newly formed during a starburst episode in a *bulge* induced mainly by galaxy mergers, $\Delta M_{\rm BH}$ is the total SMBH mass growth,

[9] Changing the seed BH mass to $10^5\,M_\odot$ does not affect the results at the high-$M_{\rm BH}$ or high-$M_{\rm bulge}$ regions, primarily because the ν^2GC model allows super-Eddington accretion (Shirakata et al. 2016).

and $f_{\rm BH}$ is a constant (=0.01) selected to match the local $M_{\rm BH}$–$M_{\rm bulge}$ relation. It is thus apparent that the simulated galaxies tend to follow the local relation. Note that we use $M_{\rm dyn}$ returned by the model, which indicates either (i) total mass within a half-mass radius (bulge-dominated galaxy) or (ii) total mass within a disk effective radius (disk-dominated galaxy). The mass of the dark matter would not be important at these spatial scales (Genzel et al. 2017). Thus, our comparison with observed data is fair.

It is intriguing in figure 9 that $M_{\rm BH}$ and $M_{\rm dyn}$ of the low-luminosity quasars (HSC + CFHQS) are close to the simulated values. This implies, based on the ν^2GC model, that these quasars could have been formed through the standard, (quasi-)synchronized galaxy–SMBH formation scenario (e.g., Di Matteo et al. 2005; Hopkins et al. 2006), although we cannot exclude other evolutionary scenarios. That the $M_{\rm BH}$ of J0859+0022 is significantly lower ($\sim 2 \times 10^7\,M_\odot$) than the local relation seems to support that standard galaxy evolutionary scheme, where a starburst phase (or growth of stellar content) occurs earlier and an SMBH growth happens later (see also a recent ALMA work by Ueda et al. 2018). Note that expected halo masses are $\sim$ several $\times\ 10^{12}\,M_\odot$ for those lower-mass quasars based on our model, which will be observationally tested in future.

On the other hand, it is still challenging to form massive-end *galaxies* ($M_{\rm dyn} \gtrsim 10^{11}\,M_\odot$) that contain $M_{\rm BH} \gtrsim 5 \times 10^8\,M_\odot$ SMBHs with this ν^2GC simulation. We would also point out that the scatter around the local relation is smaller at $M_{\rm dyn} \gtrsim 10^{11}\,M_\odot$, likely indicating (several episodes of) AGN feedbacks are regulating galaxy growth, converging finally to the local relation. As such massive-end objects should be quite rare, this remains a room that we will be able to generate those objects once we simulate much larger volumes. It is, however, virtually impossible to form quasars having $M_{\rm dyn} \lesssim 10^{11}\,M_\odot$ and $M_{\rm BH} \gtrsim 5 \times 10^8\,M_\odot$ with our model, as long as we use the fixed $f_{\rm BH}$. One other possibility is that these over-massive objects were formed through different path(s) from those incorporated in the ν^2GC simulation. For example, an additional supply of cold gas directly from the intergalactic medium would boost the mass, especially in the nuclear region of galaxies (e.g., Dekel et al. 2009): the potential importance of fueling mechanisms other than the standard merger picture has been investigated recently (e.g., Trakhtenbrot et al. 2017). It is even plausible that such quasars with over-massive SMBHs will accordingly evolve into *galaxies with over-massive SMBHs* at $z \sim 0$, which have begun to be found recently (van den Bosch et al. 2012), although dry mergers will move them toward the local relation as time goes by from $z \sim 6$ to $\sim$0. Further investigations of galaxy properties as well as environments around the quasars are essential to understand better the underlying processes of co-evolution.

5 Summary and future prospects

We have presented ALMA observations of four optically low-luminosity ($M_{1450} > -25$) quasars at $z \gtrsim 6$ recently discovered by our wide and deep optical survey with the Hyper Suprime-Cam (HSC) on the Subaru telescope (Matsuoka et al. 2016). This study significantly increased the known sample in the low-luminosity regime at $z \gtrsim 6$ already reported in works of Willott et al. (2013, 2015, 2017), giving us a less-biased view of high-redshift galaxy–SMBH evolution. All four quasars have been detected in the [C II] emission line and the underlying rest-FIR continuum emission. The main findings of this paper can be summarized as follows.

1. The [C II] line fluxes are as low as 0.4–1.1 Jy km s^{-1}, which corresponds to line luminosities of $L_{\rm [C\,II]} \simeq (4\text{–}10) \times 10^8\,L_\odot$. These are more than one order of magnitude fainter than in $z \gtrsim 6$ optically-luminous quasars (e.g., Wang et al. 2013; Venemans et al. 2016), and are comparable to local LIRGs (Díaz-Santos et al. 2013). The line FWHM ranges from 192 to 356 km s^{-1}, similar to other $z \gtrsim 6$ quasars (e.g., Wang et al. 2013; Willott et al. 2015; Venemans et al. 2016). The inferred star formation rates are similarly low (SFR $\sim$ 25–67 $M_\odot$ yr^{-1}) as compared to the luminous quasar hosts (>100 $M_\odot$ yr^{-1}).
2. The underlying rest-FIR continuum emission was detected in all objects (136–246 μJy beam^{-1}). A modified blackbody fit with a dust temperature $T_{\rm d} = 47$ K to the measurements yielded FIR luminosities $L_{\rm FIR} \simeq (3\text{–}5) \times 10^{11}\,L_\odot$, i.e., LIRG-class $L_{\rm FIR}$. Meanwhile, we found that $T_{\rm d} = 35$ K [$L_{\rm FIR} \simeq (1\text{–}2) \times 10^{11}\,L_\odot$] yields IR-based SFR (23–40 $M_\odot$ yr^{-1}) that better match the [C II]-based SFR. In either case, the inferred dust masses are several $\times\ 10^7\,M_\odot$, which are an order of magnitude smaller than the optically-luminous quasar host galaxies at $z \gtrsim 6$ (e.g., Wang et al. 2007; Venemans et al. 2016).
3. The spatial extent of the barely resolved [C II] emitting regions are mostly $\sim$3 kpc for the HSC quasars (J2216−0016 shows $\sim$5 kpc), which agrees with the continuum-derived sizes despite the large errors. These numbers are comparable to those of the optically-luminous quasars having at least an order of magnitude higher $L_{\rm FIR}$ (or dust mass). It thus implies that the correspondingly different ISM mass surface density (Hopkins & Quataert 2010) drives the difference in AGN activity between the HSC quasars and the more luminous quasars.

4. We did not find any continuum or line emitter physically close to the HSC quasars within the nominal FoVs, except for one likely lower-redshift weak line emitter. Recent number counts suggest that we could have seen some objects in our deep observations (5σ = 44–104 μJy beam^{-1}), but several factors could reconcile this discrepancy.
5. The BAL quasar J2216−0016 seems to show two components in the [C II] emission line spectrum and its velocity-integrated spatial distribution. This may reflect either [C II]-outflows or a galaxy merger. Higher resolution observations are required to further elucidate the nature of this high-redshift BAL quasar host.
6. The $L_{[\mathrm{C\,II}]}/L_{\mathrm{FIR}}$ ratios of the HSC quasars are fully consistent with the local LIRG-class objects, whereas optically-luminous quasars tend to show a [C II]-deficit trend at increasing L_{FIR}. This suggests that a star formation mode similar to local LIRGs (not ULIRG-like bursts) prevails in the HSC quasars. The order of magnitude of difference in the SFR (and likely ISM mass) surface densities between the HSC quasars and optically-luminous quasars may be the one of the physical origin(s) of the deficit.
7. Our attempt to place the HSC quasars on the stellar mass (M_*; we used dynamical masses M_{dyn} as surrogates for them) vs. SFR plane suggests that the HSC quasars and other similarly less-luminous quasars are on or even below the $z \sim 6$ star formation main sequence (MS), i.e., they are now ceasing their star formation. This is supported by both recent observations and a semi-analytical galaxy evolution model (ν^2GC, Makiya et al. 2016). As optically-luminous quasars reside on or even above the MS (i.e., starburst galaxies), there could be an evolutionary difference between these luminous and less-luminous quasar hosts.
8. Our dynamical measurements suggest that the HSC quasars along with similarly less-luminous quasars at $z \gtrsim 6$ (e.g., Willott et al. 2015, 2017) tend to follow the local co-evolutionary relation, whereas luminous objects show clear departures from it (over-massive SMBHs), particularly at $M_{\mathrm{dyn}} < 10^{11}\,M_{\odot}$. This highlights the importance of probing less-luminous quasars to depict the unbiased shape of the early co-evolution. The mass properties of those less-luminous quasars can be reproduced by the ν^2GC model, implying they could be formed with quasi-synchronized galaxy (bulge)–SMBH evolution scheme, although we do not argue that this is the only scenario to explain the results. On the other hand, we may need to consider some other evolution paths to generate galaxies hosting over-massive SMBHs.

A higher spatial resolution that that provided in this study (∼0.″5), which is achievable with ALMA, is necessary to elucidate the physical origin of the spectral peculiarity of J2216−0016. Furthermore, the trends of low-luminosity quasars shown above, which are clearly different from those of optically-luminous quasars, are based on the small sample. This will be statistically confirmed with our growing SHELLQs sample.

Acknowledgments

We thank the anonymous referee for his/her thorough reading and useful comments which greatly improved this paper. T.I. particularly thanks Dr. T. Suzuki at NAOJ for their fruitful discussion. This paper makes use of the following ALMA data: ADS/JAO.ALMA#2016.1.01423.S. ALMA is a partnership of ESO (representing its member states), NSF (USA) and NINS (Japan), together with NRC (Canada), NSC and ASIAA (Taiwan), and KASI (Republic of Korea), in cooperation with the Republic of Chile. The Joint ALMA Observatory is operated by ESO, AUI/ NRAO and NAOJ.

The Hyper Suprime-Cam (HSC) collaboration includes the astronomical communities of Japan and Taiwan, and Princeton University. The HSC instrumentation and software were developed by the National Astronomical Observatory of Japan (NAOJ), the Kavli Institute for the Physics and Mathematics of the Universe (Kavli IPMU), the University of Tokyo, the High Energy Accelerator Research Organization (KEK), the Academia Sinica Institute for Astronomy and Astrophysics in Taiwan (ASIAA), and Princeton University. Funding was contributed by the FIRST program from Japanese Cabinet Office, the Ministry of Education, Culture, Sports, Science and Technology (MEXT), the Japan Society for the Promotion of Science (JSPS), Japan Science and Technology Agency (JST), the Toray Science Foundation, NAOJ, Kavli IPMU, KEK, ASIAA, and Princeton University.

This paper makes use of software developed for the Large Synoptic Survey Telescope. We thank the LSST Project for making their code available as free software at ⟨http://dm.lsstcorp.org⟩.

The Pan-STARRS1 Surveys (PS1) have been made possible through contributions of the Institute for Astronomy, the University of Hawaii, the Pan-STARRS Project Office, the Max-Planck Society and its participating institutes, the Max Planck Institute for Astronomy, Heidelberg and the Max Planck Institute for Extraterrestrial Physics, Garching, The Johns Hopkins University, Durham University, the University of Edinburgh, Queen's University Belfast, the Harvard-Smithsonian Center for Astrophysics, the Las Cumbres Observatory Global Telescope Network Incorporated, the National Central University of Taiwan, the Space Telescope Science Institute, the National Aeronautics and Space Administration under Grant No. NNX08AR22G issued through the Planetary Science Division of the NASA Science Mission Directorate, the National Science Foundation under Grant No. AST-1238877, the University of Maryland, and Eotvos Lorand University (ELTE).

T.I., M.O., K.K, N.K., H.U., R.M., and T.N. are supported by JSPS KAKENHI grant numbers 17K14247 (T.I.), 15J02115 (M.O.), 17H06130 (K.K.), 15H03645 (N.K.), 17K14252 (H.U.), 15H05896 (R.M.), 16H01101, 16H03958, and 17H01114 (T.N.), respectively. H.S. has been supported by the Sasakawa Scientific

Research Grant from the Japan Science Society (29-214). T.I. is supported by the ALMA Japan Research Grant of NAOJ Chile Observatory, NAOJ-ALMA-175.

References

Aalto, S., García-Burillo, S., Muller, S., Winters, J. M., van der Werf, P., Henkel, C., Costagliola, F., & Neri, R. 2012, A&A, 537, A44

Abel, N. P., Dudley, C., Fischer, J., Satyapal, S., & van Hoof, P. A. M. 2009, ApJ, 701, 1147

Alton, P. B., Xilouris, E. M., Misiriotis, A., Dasyra, K. M., & Dumke, M. 2004, A&A, 425, 109

Aravena, M., et al. 2016, ApJ, 833, 68

Bañados, E., et al. 2014, AJ, 148, 14

Bañados, E., et al. 2016, ApJS, 227, 11

Bañados, E., et al. 2018, Nature, 553, 473

Bañados, E., Decarli, R., Walter, F., Venemans, B. P., Farina, E. P., & Fan, X. 2015, ApJ, 805, L8

Beelen, A., Cox, P., Benford, D. J., Dowell, C. D., Kovács, A., Bertoldi, F., Omont, A., & Carilli, C. L. 2006, ApJ, 642, 694

Bertoldi, F., Carilli, C. L., Cox, P., Fan, X., Strauss, M. A., Beelen, A., Omont, A., & Zylka, R. 2003a, A&A, 406, L55

Bertoldi, F., et al. 2003b, A&A, 409, L47

Brauher, J. R., Dale, D. A., & Helou, G. 2008, ApJS, 178, 280

Calura, F., Gilli, R., Vignali, C., Pozzi, F., Pipino, A., & Matteucci, F. 2014, MNRAS, 438, 2765

Capak, P. L., et al. 2015, Nature, 522, 455

Carilli, C. L., et al. 2001, ApJ, 555, 625

Carilli, C. L., & Walter, F. 2013, ARA&A, 51, 105

Carnall, A. C., et al. 2015, MNRAS, 451, L16

Chapman, S. C., Blain, A. W., Smail, I., & Ivison, R. J. 2005, ApJ, 622, 772

Chen, C.-T. J., et al. 2013, ApJ, 773, 3

Cicone, C., et al. 2014, A&A, 562, A21

Cicone, C., et al. 2015, A&A, 574, A14

Coppin, K., et al. 2008, MNRAS, 384, 1597

da Cunha, E., et al. 2013, ApJ, 766, 13

Daddi, E., et al. 2007, ApJ, 670, 156

De Breuck, C., Maiolino, R., Caselli, P., Coppin, K., Hailey-Dunsheath, S., & Nagao, T. 2011, A&A, 530, L8

Decarli, R., et al. 2017, Nature, 545, 457

Decarli, R., et al. 2018, ApJ, 854, 97

Dekel, A., et al. 2009, Nature, 457, 451

De Looze, I., Baes, M., Bendo, G. J., Cortese, L., & Fritz, J. 2011, MNRAS, 416, 2712

De Rosa, G., et al. 2014, ApJ, 790, 145

Díaz-Santos, T., et al. 2013, ApJ, 774, 68

Di Matteo, T., Springel, V., & Hernquist, L. 2005, Nature, 433, 604

Draine, B. T., et al. 2007, ApJ, 663, 866

Dunlop, J. S., et al. 2017, MNRAS, 466, 861

Eilers, A.-C., Davies, F. B., Hennawi, J. F., Prochaska, J. X., Lukić, Z., & Mazzucchelli, C. 2017, ApJ, 840, 24

Elbaz, D., et al. 2007, A&A, 468, 33

Enoki, M., Ishiyama, T., Kobayashi, M. A. R., & Nagashima, M. 2014, ApJ, 794, 69

Fan, X., et al. 2003, AJ, 125, 1649

Fan, X., et al. 2006, AJ, 131, 1203

Farrah, D., et al. 2013, ApJ, 776, 38

Farrah, D., Lacy, M., Priddey, R., Borys, C., & Afonso, J. 2007, ApJ, 662, L59

Ferrarese, L., & Merritt, D. 2000, ApJ, 539, L9

Feruglio, C., et al. 2017, A&A, 608, A30

Fujimoto, S., Ouchi, M., Ono, Y., Shibuya, T., Ishigaki, M., Nagai, H., & Momose, R. 2016, ApJS, 222, 1

Fujimoto, S., Ouchi, M., Shibuya, T., & Nagai, H. 2017, ApJ, 850, 83

Furusawa, H., et al. 2018, PASJ, 70, S3

Gallerani, S., Fan, X., Maiolino, R., & Pacucci, F. 2017, PASA, 34, e022

Gallerani, S., Ferrara, A., Neri, R., & Maiolino, R. 2014, MNRAS, 445, 2848

Gehrels, N. 1986, ApJ, 303, 336

Genzel, R., et al. 2017, Nature, 543, 397

Graciá-Carpio, J., et al. 2011, ApJ, 728, L7

Grazian, A., et al. 2015, A&A, 575, A96

Greene, J. E., Zakamska, N. L., & Smith, P. S. 2012, ApJ, 746, 86

Gullberg, B., et al. 2015, MNRAS, 449, 2883

Harikane, Y., et al. 2017, arXiv:1711.03735

Helou, G., Khan, I. R., Malek, L., & Boehmer, L. 1988, ApJS, 68, 151

Herrera-Camus, R., et al. 2015, ApJ, 800, 1

Hirashita, H., & Voshchinnikov, N. V. 2014, MNRAS, 437, 1636

Hollenbach, D. J., & Tielens, A. G. G. M. 1999, Rev. Mod. Phys., 71, 173

Hopkins, P. F., Hernquist, L., Cox, T. J., Di Matteo, T., Robertson, B., & Springel, V. 2006, ApJS, 163, 1

Hopkins, P. F., Hernquist, L., Cox, T. J., & Kereš, D. 2008, ApJS, 175, 356

Hopkins, P. F., & Quataert, E. 2010, MNRAS, 407, 1529

Ikarashi, S., et al. 2015, ApJ, 810, 133

Ishiyama, T., Enoki, M., Kobayashi, M. A. R., Makiya, R., Nagashima, M., & Oogi, T. 2015, PASJ, 67, 61

Ivison, R. J., et al. 2010, A&A, 518, L35

Jiang, L., et al. 2016, ApJ, 833, 222

Kashikawa, N., et al. 2015, ApJ, 798, 28

Kaufman, M. J., Wolfire, M. G., Hollenbach, D. J., & Luhman, M. L. 1999, ApJ, 527, 795

Kaviraj, S. 2014, MNRAS, 440, 2944

Kawanomoto, S., et al. 2017, PASJ, submitted

Kennicutt, R. C., Jr. 1998, ARA&A, 36, 189

Komiyama, Y., et al. 2018, PASJ, 70, S2

Kormendy, J., & Ho, L. C. 2013, ARA&A, 51, 511

Kovács, A., Chapman, S. C., Dowell, C. D., Blain, A. W., Ivison, R. J., Smail, I., & Phillips, T. G. 2006, ApJ, 650, 592

Krogager, J.-K., Zirm, A. W., Toft, S., Man, A., & Brammer, G. 2014, ApJ, 797, 17

Kroupa, P. 2001, MNRAS, 322, 231

Lamastra, A., Menci, N., Maiolino, R., Fiore, F., & Merloni, A. 2010, MNRAS, 405, 29

Langer, W. D., & Pineda, J. L. 2015, A&A, 580, A5

Lauer, T. R., Tremaine, S., Richstone, D., & Faber, S. M. 2007, ApJ, 670, 249

Leipski, C., et al. 2014, ApJ, 785, 154

Li, Y., et al. 2007, ApJ, 665, 187

Luhman, M. L., Satyapal, S., Fischer, J., Wolfire, M. G., Sturm, E., Dudley, C. C., Lutz, D., & Genzel, R. 2003, ApJ, 594, 758
Lutz, D., et al. 2010, ApJ, 712, 1287
Lyu, J., & Rieke, G. H. 2017, ApJ, 841, 76
McMullin, J. P., Waters, B., Schiebel, D., Young, W., & Golap, K. 2007, in ASP Conf. Ser., 376, Astronomical Data Analysis Software and Systems XVI, ed. R. A. Shaw et al. (San Francisco: ASP), 127
Madau, P., & Dickinson, M. 2014, ARA&A, 52, 415
Maiolino, R., et al. 2005, A&A, 440, L51
Maiolino, R., et al. 2012, MNRAS, 425, L66
Maiolino, R., Caselli, P., Nagao, T., Walmsley, M., De Breuck, C., & Meneghetti, M. 2009, A&A, 500, L1
Makiya, R., et al. 2016, PASJ, 68, 25
Malhotra, S., et al. 1997, ApJ, 491, L27
Mancini, M., Schneider, R., Graziani, L., Valiante, R., Dayal, P., Maio, U., Ciardi, B., & Hunt, L. K. 2015, MNRAS, 451, L70
Marconi, A., & Hunt, L. K. 2003, ApJ, 589, L21
Matsuoka, Y., et al. 2016, ApJ, 828, 26
Matsuoka, Y., et al. 2018, PASJ, 70, S35
Mazzucchelli, C., et al. 2017, ApJ, 849, 91
Mechtley, M., et al. 2012, ApJ, 756, L38
Michałowski, M. J., Murphy, E. J., Hjorth, J., Watson, D., Gall, C., & Dunlop, J. S. 2010, A&A, 522, A15
Miyazaki, S., et al. 2012, Proc. SPIE, 8446, 84460Z
Miyazaki, S., et al. 2018, PASJ, 70, S1
Mortlock, D. J., et al. 2009, A&A, 505, 97
Mortlock, D. J., et al. 2011, Nature, 474, 616
Murphy, E. J., et al. 2011, ApJ, 737, 67
Nagao, T., Maiolino, R., De Breuck, C., Caselli, P., Hatsukade, B., & Saigo, K. 2012, A&A, 542, L34
Narayanan, D., & Krumholz, M. R. 2017, MNRAS, 467, 50
Nesvadba, N. P. H., Lehnert, M. D., De Breuck, C., Gilbert, A. M., & van Breugel, W. 2008, A&A, 491, 407
Omont, A., Willott, C. J., Beelen, A., Bergeron, J., Orellana, G., & Delorme, P. 2013, A&A, 552, A43
Oteo, I., Zwaan, M. A., Ivison, R. J., Smail, I., & Biggs, A. D. 2016, ApJ, 822, 36
Petric, A. O., Carilli, C. L., Bertoldi, F., Fan, X., Cox, P., Strauss, M. A., Omont, A., & Schneider, D. P. 2003, AJ, 126, 15
Popping, G., Somerville, R. S., & Galametz, M. 2017, MNRAS, 471, 3152
Priddey, R. S., Isaak, K. G., McMahon, R. G., Robson, E. I., & Pearson, C. P. 2003, MNRAS, 344, L74
Priddey, R. S., Ivison, R. J., & Isaak, K. G. 2008, MNRAS, 383, 289
Reed, S. L., et al. 2017, MNRAS, 468, 4702
Richards, G. T., et al. 2006, ApJS, 166, 470
Riechers, D. A., et al. 2013, Nature, 496, 329
Robson, I., Priddey, R. S., Isaak, K. G., & McMahon, R. G. 2004, MNRAS, 351, L29
Salmon, B., et al. 2015, ApJ, 799, 183
Salpeter, E. E. 1964, ApJ, 140, 796
Sargsyan, L., Samsonyan, A., Lebouteiller, V., Weedman, D., Barry, D., Bernard-Salas, J., Houck, J., & Spoon, H. 2014, ApJ, 790, 15
Schramm, M., & Silverman, J. D. 2013, ApJ, 767, 13
Schulze, A., & Wisotzki, L. 2014, MNRAS, 438, 3422
Schweitzer, M., et al. 2006, ApJ, 649, 79
Shao, Y., et al. 2017, ApJ, 845, 138
Shen, Y., Greene, J. E., Strauss, M. A., Richards, G. T., & Schneider, D. P. 2008, ApJ, 680, 169
Shirakata, H., et al. 2016, MNRAS, 461, 4389
Shirakata, H., et al. 2018, arXiv:1802.02169
Shirakata, H., Okamoto, T., Enoki, M., Nagashima, M., Kobayashi, M. A. R., Ishiyama, T., & Makiya, R. 2015, MNRAS, 450, L6
Silva, A., Sajina, A., Lonsdale, C., & Lacy, M. 2015, ApJ, 806, L25
Simpson, J. M., et al. 2015, ApJ, 807, 128
Solomon, P. M., & Vanden Bout, P. A. 2005, ARA&A, 43, 677
Somerville, R. S., & Davé, R. 2015, ARA&A, 53, 51
Somerville, R. S., Hopkins, P. F., Cox, T. J., Robertson, B. E., & Hernquist, L. 2008, MNRAS, 391, 481
Speagle, J. S., Steinhardt, C. L., Capak, P. L., & Silverman, J. D. 2014, ApJS, 214, 15
Stacey, G. J., Geis, N., Genzel, R., Lugten, J. B., Poglitsch, A., Sternberg, A., & Townes, C. H. 1991, ApJ, 373, 423
Stacey, G. J., Hailey-Dunsheath, S., Ferkinhoff, C., Nikola, T., Parshley, S. C., Benford, D. J., Staguhn, J. G., & Fiolet, N. 2010, ApJ, 724, 957
Stefan, I. I., et al. 2015, MNRAS, 451, 1713
Steinhardt, C. L., & Speagle, J. S. 2014, ApJ, 796, 25
Straatman, C. M. S., et al. 2014, ApJ, 783, L14
Straatman, C. M. S., et al. 2015, ApJ, 808, L29
Strandet, M. L., et al. 2017, ApJ, 842, L15
Symeonidis, M. 2017, MNRAS, 465, 1401
Symeonidis, M., Giblin, B. M., Page, M. J., Pearson, C., Bendo, G., Seymour, N., & Oliver, S. J. 2016, MNRAS, 459, 257
Tanaka, M. 2015, ApJ, 801, 20
Tanaka, M., et al. 2018, PASJ, 70, S9
Taniguchi, Y. 1999, ApJ, 524, 65
Targett, T. A., Dunlop, J. S., & McLure, R. J. 2012, MNRAS, 420, 3621
Tasca, L. A. M., et al. 2015, A&A, 581, A54
Tateuchi, K., et al. 2015, ApJS, 217, 1
Toba, Y., Bae, H.-J., Nagao, T., Woo, J.-H., Wang, W.-H., Wagner, A. Y., Sun, A.-L., & Chang, Y.-Y. 2017, ApJ, 850, 140
Toft, S., et al. 2014, ApJ, 782, 68
Trakhtenbrot, B., Lira, P., Netzer, H., Cicone, C., Maiolino, R., & Shemmer, O. 2017, ApJ, 836, 8
Trump, J. R., et al. 2006, ApJS, 165, 1
U, V., et al. 2012, ApJS, 203, 9
Ueda, Y., et al. 2018, ApJ, 853, 24
Umehata, H., et al. 2017, ApJ, 835, 98
Valiante, R., Agarwal, B., Habouzit, M., & Pezzulli, E. 2017, PASA, 34, e031
Valiante, R., Schneider, R., Salvadori, S., & Gallerani, S. 2014, MNRAS, 444, 2442
van den Bosch, R. C. E., Gebhardt, K., Gültekin, K., van de Ven, G., van der Wel, A., & Walsh, J. L. 2012, Nature, 491, 729
van Dokkum, P. G., et al. 2008, ApJ, 677, L5
Venemans, B. P., et al. 2012, ApJ, 751, L25
Venemans, B. P., et al. 2013, ApJ, 779, 24
Venemans, B. P., et al. 2015a, ApJ, 801, L11
Venemans, B. P., et al. 2015b, MNRAS, 453, 2259
Venemans, B. P., et al. 2017, ApJ, 851, L8

Venemans, B. P., Walter, F., Zschaechner, L., Decarli, R., De Rosa, G., Findlay, J. R., McMahon, R. G., & Sutherland, W. J. 2016, ApJ, 816, 37
Vestergaard, M., & Osmer, P. S. 2009, ApJ, 699, 800
Volonteri, M. 2012, Science, 337, 544
Volonteri, M., Capelo, P. R., Netzer, H., Bellovary, J., Dotti, M., & Governato, F. 2015, MNRAS, 449, 1470
Wagg, J., et al. 2012, ApJ, 752, L30
Walter, F., Carilli, C., Bertoldi, F., Menten, K., Cox, P., Lo, K. Y., Fan, X., & Strauss, M. A. 2004, ApJ, 615, L17
Wang, F., et al. 2017, ApJ, 839, 27
Wang, R., et al. 2007, AJ, 134, 617
Wang, R., et al. 2008, ApJ, 687, 848
Wang, R., et al. 2010, ApJ, 714, 699
Wang, R., et al. 2011a, AJ, 142, 101
Wang, R., et al. 2011b, ApJ, 739, L34
Wang, R., et al. 2013, ApJ, 773, 44
Wang, R., et al. 2016, ApJ, 830, 53
Weymann, R. J., Morris, S. L., Foltz, C. B., & Hewett, P. C. 1991, ApJ, 373, 23
Whitaker, K. E., van Dokkum, P. G., Brammer, G., & Franx, M. 2012, ApJ, 754, L29
Williams, J. P., de Geus, E. J., & Blitz, L. 1994, ApJ, 428, 693
Willott, C. J., et al. 2007, AJ, 134, 2435
Willott, C. J., et al. 2009, AJ, 137, 3541
Willott, C. J., et al. 2010a, AJ, 139, 906
Willott, C. J., et al. 2010b, AJ, 140, 546
Willott, C. J., Bergeron, J., & Omont, A. 2015, ApJ, 801, 123
Willott, C. J., Bergeron, J., & Omont, A. 2017, ApJ, 850, 108
Willott, C. J., McLure, R. J., & Jarvis, M. J. 2003, ApJ, 587, L15
Willott, C. J., Omont, A., & Bergeron, J. 2013, ApJ, 770, 13
Willott, C. J., Percival, W. J., McLure, R. J., Crampton, D., Hutchings, J. B., Jarvis, M. J., Sawicki, M., & Simard, L. 2005, ApJ, 626, 657
Wu, X.-B., et al. 2015, Nature, 518, 512
Yamaguchi, Y., et al. 2017, ApJ, 845, 108
Yang, G., et al. 2017, ApJ, 842, 72
Yun, M. S., Carilli, C. L., Kawabe, R., Tutui, Y., Kohno, K., & Ohta, K. 2000, ApJ, 528, 171